DYNAMICAL AND STATISTICAL FRAGMENT PRODUCTION IN HEAVY-ION COLLISIONS AT INTERMEDIATE ENERGIES

W. Gawlikowicz

Heavy-Ion Laboratory, Warsaw University
Pasteura 5A, 02-093 Warszawa, Poland

(Received March 18, 2009)

A large set of experimental data was analyzed in terms of characteristic signatures of different interaction as well as product emission scenarios. The analysis confirms that the reaction cross-section appears still dominated by dissipative binary reactions involving the survival of well-defined projectile- and target-like fragments. Consistent with such a "gentle" collision scenario are the Galilei-invariant velocity distributions of charged products featuring statistical emission from two fully accelerated projectile- and target-like fragments. On the other hand, the Galilei-invariant velocity plots reveal the presence of a third effective emission source with velocity intermediate between the velocities of projectile- and target-like fragments. Fragments emitted from the intermediate-velocity source appear to be produced *dynamically* in the overlap zone of the projectile and target nuclei. The experimental multidimensional joint distributions of neutrons and charged reaction products were found to exhibit several different types of prominent correlation patterns. It makes them a useful tool for probing reactions scenarios, different from the traditional approach of interpreting inclusive yields of individual reaction products.

PACS numbers: 25.70.Pq, 25.70.Mn

1. Introduction

Nuclear research in the past half century has been strongly concentrated on explanation of mechanisms of particle emission from hot nuclei. The research has covered wide range of possible bombarding energies, from those close to interaction barrier (few MeV/nucleon), to relativistic collisions (few hundred MeV/nucleon).

Heavy-ion reactions at bombarding energies near the interaction barrier are characterized by stochastic exchange of nucleons between colliding projectile and target nuclei. This process is explained satisfactorily by one-

body (mean-field) transport phenomena and one-body dissipation mechanisms [1]. The stochastic nucleon-exchange mechanism explains qualitatively experimentally measured mass and charge distributions of massive reaction partners, correlated with their excitation energies and spins [2]. In such a reaction picture, the nucleon-exchange process, together with nuclear and Coulomb potential interaction between colliding ions, dissipates the kinetic energy of relative motion of reaction partners, as the dinuclear system rotates about its center of gravity. The dinuclear system is mechanically unstable and subsequently re-separates due to repulsive Coulomb and centrifugal forces, forming excited projectile-like (PLF) and target-like (TLF) fragments in the reaction exit channel. Since the PLF and TLF are excited, they decay subsequently via particle evaporation and/or fission. As an alternative, a composite system can be formed, usually, in an incomplete fusion of projectile and target nuclei. The composite system deexcitation process is the same as for PLF and TLF.

The reaction picture is quite different at high bombarding energies (few hundred MeV/nucleon). Here the collision dynamics is mainly governed by direct nucleon–nucleon interaction (two-body dissipation). Because of the high relative velocity of colliding nucleons the repulsive part of the nuclear potential becomes dominant. The mean-field effects (one-body dissipation) could be then neglected, as it is assumed in the Intranuclear Cascade Model (INC) [3], an often used theoretical approach in this bombarding energy range. Because of the high relative velocity of colliding ions, the reaction time is too small to allow forming of dinuclear system. After direct multinucleon-exchange process hot fragments are formed, deexciting afterwards via prompt and/or sequential particle emission. Since the mean-field effects can be neglected, as compared to nucleon–nucleon interaction, there is no possibility for composite system forming at high bombarding energies. A characteristic feature at high bombarding energies is the particle production (especially pions), not present at low bombarding energies.

Comparing reaction pictures for low and high bombarding energies, one can find, that the heavy-ion reactions at intermediate (Fermi) bombarding energies (20–100 MeV/nucleon) have features characteristic for low bombarding energies (one-body dissipation, dissipative orbiting), as well as those for high bombarding energies (two-body dissipation, pions production). This fact makes Fermi bombarding energies an interesting research region. It makes it also difficult to interpret. Because of mixing of one- and two-body dissipation one can not separate respective time scales for intrinsic and collective degrees of freedom. Moreover, since in Fermi energy region the energy relaxation time ($\approx$ 20–40 fm/c) becomes comparable with macroscopic motion time, the interpretation in terms of statistical thermodynamics becomes difficult.

In the entire range of possible bombarding energies, the interpretation of heavy-ion reaction mechanism is based on observed particle emission. The evolution of particle yield with bombarding energy can be described as follows. At low bombarding energies, one observes emission of neutrons and light-charged particles (LCP) [2] from excited primary PLF and TLF. With increasing bombarding energy or collision centrality, one begins to observe additionally emission of intermediate-mass fragments (IMFs) [4], which are seen to account for a considerable fraction of the system mass/energy for more central collisions [4–6]. In the associated reaction scenario, the reaction cross-section is dominated by dissipative binary collisions, with well defined projectile- and target-like fragments (PLF and TLF) [2]. The observed particle yield is then to a large extent associated with statistical emission from these two fragments, excited in the course of their mutual interaction. Additionally, for central collisions at low bombarding energies the fusion of projectile and target is possible. This process, however, accounts for a small fraction of reaction cross-section.

The emission of intermediate-mass fragments increases rapidly for bombarding energies in the range of 15–20 MeV/nucleon, depending on the colliding system. The rapid increase of fragments emission accompanied by copious IMF production is known in the literature as *multifragmentation* [7–9]. It is frequently interpreted in terms of nuclear liquid-gas phase transition [10]. It is then directly related to nuclear equation of state, from which one can derive relation between such state parameters as density, temperature and pressure. It allows also to study the system evolution through such phase separation boundaries as the binodal or spinodal boundary limits [11].

There is also another interpretation of nuclear multifragmentation, related to fluctuations and instabilities in the excited nuclear systems [12]. The multifragmentation process is here connected with instabilities in the dynamical evolution of the system created in heavy-ion collisions. It was shown, that the Coulomb [13] or spinodal [14] type of instabilities may also lead to the fragmentation of an excited system.

With further increase of bombarding energy, the description of the heavy-ion collisions changes, and a new source of emitted fragments appears — the intermediate-velocity source (IVS), which moves with a velocity intermediate between the velocities of PLF and TLF [15]. In the associated reaction description, the fragment yield has three components associated with the decay of PLF, TLF, and IVS. While the emission from excited PLF and TLF exhibits *statistical* decay pattern from thermal emission source, the IVS emission exhibits *dynamical* character as an effect of clusterization process. In the above picture of intermediate-energy collisions, the IVS emission is related to the overlap region of projectile and target, which forms a participant matter. In consequence, the IMF multiplicity is increasing with the collision centrality, as projectile-target overlap region increases too.

The appearance of IVS changes a point of view on the character of multifragmentation processes at intermediate energies. The observed fragment yield has components from different reaction mechanisms. The description of multifragmentation has to be related then to proper selection of emission sources. The dynamical IVS component complicates the distinction between prompt and sequential scenarios of statistical multifragmentation, as it overlaps with statistical emission from the excited PLF and TLF sources.

2. Theoretical models in the Fermi energy domain

The description of nuclear collisions is given by time-dependent, n-body Schrödinger equation:

$$i\hbar \frac{\partial \psi^{(n)}}{\partial t} = H^{(n)} \psi^{(n)} \,, \tag{2.1}$$

where $\psi^{(n)}$ is n-body wave function, and $H^{(n)}$ is a n-body Hamiltonian. Since this equation cannot be solved in the case of complex systems, such as a system of colliding heavy-ions, the theoretical modeling of heavy-ion collisions is based on strong simplifications. They can be characterized by different treatment of nuclear quantum properties and the manner in which the system evolution is calculated. The distinct approaches include here:

- **TDHF** (Time dependent Hartree–Fock) models [16] suitable for relatively low collision energies (up to $\approx 10\,\mathrm{MeV/u}$) and based on the assumption that the mean free path of nucleons is greater than the size of nucleus. They offer a "real" quantum approach, where the system behavior is determined by the evolution of anti-symmetrized wave functions, consistent with the Pauli exclusion principle.

- **Nuclear transport** models (Boltzmann–Übling–Uhlenbeck (BUU) [17], Vlasov–Übling–Uhlenbeck (VUU) [18], Boltzmann–Nordheim –Vlasov (BNV) [19], and Boltzmann–Langevin (BL) [20]), considering the evolution of the population function of the six-dimensional (geometrical and momentum) phase space under action of inertial and (one-body) mean-field forces, with an account of (two- and more- body) nucleon–nucleon interactions. One can then calculate the nuclear matter density distribution in a very straightforward way, by integrating the population function over the momentum space. It is ultimately the nuclear matter density distribution and its time-asymptotic that can be related to experimental observables. In the above transport models, the Pauli principle is accounted for in an approximate manner.

- **Molecular dynamics** models, such as Classical Molecular Dynamics (CMD) [21], Constrained Molecular Dynamics (CoMD) [22], Quantum Molecular Dynamics (QMD) [23–25], Quasi Particle Dynamics (QPD) [26], Anti-symmetrized Molecular Dynamics (AMD) [27], Fermionic Molecular Dynamics (FMD) [28]) in which the evolution of the system is calculated using *parameterized* wave functions. Each nucleon is here represented by a wave packet with given position, width, velocity, and spin. In QMD/QPD models the Pauli principle is simulated, while FMD and AMD models are using anti-symmetrized wave functions (equivalent to Slater determinant).

Most of the heavy-ion collision models introduced above are aiming at describing the evolution of colliding systems by taking into account, to different extents, the quantum nature of atomic nuclei, with the Classical Molecular Dynamics (CMD) [21] being here an exception. In the latter approach, classical equations of motion are solved for nucleons moving in mutual field resulting from nuclear and Coulomb interactions:

$$\begin{cases} \dfrac{d\vec{r}^{(n)}}{dt} = \vec{\nabla}_p H^{(n)}(\vec{r},\vec{p})\,, \\ \dfrac{d\vec{p}^{(n)}}{dt} = -\vec{\nabla}_r H^{(n)}(\vec{r},\vec{p})\,, \end{cases} \tag{2.2}$$

where $H^{(n)}(\vec{r},\vec{p})$ is the many-body Hamiltonian of the form

$$H^{(n)}(\vec{r},\vec{p}) = \sum_{i=1}^{N} \frac{p_i^2}{2m_i} + \sum_{i<j} V(|\vec{r}_i - \vec{r}_j|)\,, \tag{2.3}$$

where N is the sum of all nucleons from projectile and target. The nucleon–nucleon potential $V(|\vec{r}|)$ may depend on particle species and, notably, is different for protons and neutrons.

Comparing the CMD and QMD models, one finds that in fact equations (2.2) and (2.3) are used in both cases, except that, CMD integrates equation of motion of *particles*, whereas QMD integrates equation of motion of *wave packets* along with simulating quantum effects. Additionally, in QMD calculations the nucleon–nucleon potential can be momentum dependent, including a Pauli potential term [23].

A different theoretical approach to heavy-ion collisions is offered by **nucleon exchange models**, such as Randrup model [29, 30], or stochastic nucleon-exchange models [31–34]. Apart from the conservative nuclear and Coulomb interaction, the nucleus–nucleus interaction is here mediated by stochastic exchange of nucleons between colliding ions, leading to formation

of projectile-like (PLF) and target-like (TLF) fragments in the reaction exit channel. Under additional assumptions, the creation of a composite system [35], or intermediate-velocity source (IVS) [36] can be considered. The nucleon exchange models can be static [30] (analytical or Monte Carlo) or include dynamics [36]. Unlike in CMD or QMD models, here the dynamical considerations are used to calculate nucleon exchange between colliding ions and, in consequence, the formation of hot sources in the reaction exit channel.

Ultimately, theoretical models of nucleus–nucleus collisions are suitable for making predictions regarding only the primary and not the final reaction products and, more specifically, regarding the prompt particles and excited fragments. In order to calculate final distribution of fragments one has to assume the deexcitation mechanism. The excited fragments deexcite via gamma or particle emission. There are two possible deexcitation processes via particle emission: *(i)* sequential binary decay — the cascade of successive binary emissions in which the particle evaporation and fission is treated in the same consistent way [37,38], and *(ii)* prompt multifragmentation — the quasi-simultaneous break-up of an excited system into many fragments [7–9]. Therefore, the full heavy-ion reaction modeling is performed using *two-step calculations*. In the first step, a **collision model** is used for calculating the properties of *primary* excited fragments. In the second step a **deexcitation model** is used to calculate the *secondary (final)* distribution of experimental observables associated with the expected reaction products.

2.1. Collision models

Since this work is focused on dynamical and statistical fragment emission in heavy-ion collisions at intermediate energies, we do not intend to characterize all individual models. Instead, we are presenting description of models used in modeling of dynamical aspects of reactions, such as nuclear transport models or quantum molecular dynamics models. On the other hand, the heavy-ion collisions are characterized also by statistical exchange of nucleons between colliding ions. Therefore, the description of models based on nucleon exchange process is also presented. A comparison between these two families of models is important for understanding the complexity of heavy-ion reactions, especially, in terms of involved reaction mechanisms.

2.1.1. Nucleon exchange models

The nucleon exchange models are based on an assumption [29], that for higher collision energies, the energy dissipation proceeds mainly through stochastic transfer of nucleons between colliding ions. The multi-nucleon transfer can be approximated by a chain of individual nucleon transfers,

assuming that the time associated with individual transfers is relatively short [30]. Under such assumptions, the heavy-ion collision can be described by the evolution of dinuclear system, where the transferred nucleons transport charge, mass, energy, linear and angular momentum.

The dynamical simulation of the nucleon transport process is done by calculating the macroscopic variables describing the properties of dinuclear system in multi-dimensional space. An exact solution can be obtained by solving the corresponding Fokker–Planck differential equation. Because such a solution would be rather cumbersome, an approximate mean-trajectory method is used instead [30]. In this method, the equations of motion for macroscopic variables are integrated along the most probable path. These equations use generalized driving forces for colliding systems A and B:

$$\begin{cases} \boldsymbol{F}^{(A)} = -\dfrac{\partial}{\partial \boldsymbol{A}} H^{(AB)}\,, \\ \boldsymbol{F}^{(B)} = -\dfrac{\partial}{\partial \boldsymbol{B}} H^{(AB)}\,, \end{cases} \tag{2.4}$$

where $H^{(AB)}$ is the macroscopic Hamiltonian of the dinuclear complex, and

$$\begin{aligned} \boldsymbol{A} &= \left(Z^{(A)}, N^{(A)}, \vec{P}^{\,(A)}, \vec{S}^{\,(A)}\right) \\ \boldsymbol{B} &= \left(Z^{(B)}, N^{(B)}, \vec{P}^{\,(B)}, \vec{S}^{\,(B)}\right) \end{aligned} \tag{2.5}$$

are the macroscopic parameters describing the system (here charge, neutron number, momentum, and spin of the two constituents of the dinuclear complex, respectively).

By modeling the dinuclear system as two Fermi–Dirac gases in contact, the system evolution, *i.e.* the nucleon transfer, can be calculated using drift and diffusion coefficients derived from driving forces. The relation between the drift and diffusion coefficients reflects the fluctuation–dissipation theorem. The macroscopic variables of the system are modified after each nucleon transfer, evolving conservatively until the subsequent transfer occurs. This means that the adiabatic transfer is assumed, *i.e.* the nucleon exchange process is assumed to be fast as compared to the time-scale of collision, and that the transferred nucleons are immediately thermalized after each transfer. In the Randrup approach, the entire nucleon exchange process is governed by one-body interaction.

In the related heavy-ion collision scenario, the dinuclear system rotates by a fraction of revolution while macroscopic kinetic energy and angular momentum are dissipated by friction-like forces arising from one-body ("window" friction) dissipation. Due to repulsive Coulomb and centrifugal forces, the dinuclear system re separates eventually into excited, quasi-equilibrated projectile-like and target-like fragments (PLF and TLF).

The ideas of Randrup and collaborators have resulted in many theoretical approaches based on stochastic exchange of nucleons between colliding heavy-ions [31–34]. In all these models, a binary exit channel scenario is assumed, *i.e.* the reaction leads always to the formation of excited PLF and TLF. The nucleon transfer between projectile and target is assumed to be dependent on the number of "activated" nucleons in the projectile and target overlap region. In the Cole random-walk model [31], the heavy-ion collision is treated as a sequence of statistically independent steps, changing the mass and charge of projectile and target. The average number of steps is taken from the Glauber theory optical limit, around the average number of nucleon–nucleon collisions, and the dispersion from corresponding Poisson distribution. The nucleon–nucleon collisions are taking place in the overlap region, along the trajectory describing relative motion of projectile and target.

The heavy-ion collisions at intermediate bombarding energies are characterized by interplay of one- and two-body dissipation. The energy dissipation process can be rather well reproduced by one-body dissipation for peripheral collisions, but should include also two-body dissipation mechanism, especially for central collisions. Both, one- and two-body dissipation mechanisms were included in the stochastic two-stage reaction Sosin model [36], which represents an extension of nucleon exchange random-walk models of Cole *et al.* [31, 32]. It also treats the heavy-ion collision as a sequence of steps. Here, the nucleon transfer is governed, on the average, by thermodynamical probabilities (related to the density of available micro-states), taking into account the fluctuations, characteristic for stochastic processes.

2.1.2. Nuclear transport models

The nuclear transport calculations are based on Bolzmann transport equation which describes the time evolution of the Wigner transform of the quantum mechanical phase-space density function $f(\vec{r},\vec{p},t)$:

$$\frac{\partial f(\vec{r},\vec{p},t)}{\partial t}+\frac{\vec{p}}{m}\vec{\nabla}_r f(\vec{r},\vec{p},t)-\vec{\nabla}U\vec{\nabla}_p f(\vec{r},\vec{p},t)=\boldsymbol{R}\,, \tag{2.6}$$

where U is the self-consistent mean-field potential. Depending on right-hand side, $\boldsymbol{R}$, the Eq. (2.6) represents one of the following approximations:

- $\boldsymbol{R}=0$ (Vlasov equation) — describing the evolution of self-consistent mean field [39] (one-body dissipation only);
- $\boldsymbol{R}=\boldsymbol{I}(f(\vec{r},\vec{p},t))$ (Landau–Vlasov equation) — Boltzmann–Übling–Uhlenbeck (BUU) [17], Vlasov–Übling-Uhlenbeck (VUU) [18], and Boltzmann–Nordheim–Vlasov (BNV) [19], approximations with collision term, $\boldsymbol{I}$, introducing two-body dissipation effects. The collision

effects are averaged after each step. The collision term contains the Pauli-blocking factor which prohibits scattering to occupied phase-space cells;

- $\boldsymbol{R} = \boldsymbol{I}(f(\vec{r},\vec{p},t)) + \delta\boldsymbol{I}(f(\vec{r},\vec{p},t))$ (Bolzmann–Langevin equation) — Bolzmann–Langevin (BL) [20] approximation with collision term, $\boldsymbol{I}$, and fluctuation term $\delta\boldsymbol{I}$, introducing stochastic effects for two-body dissipation. The quantum-statistical fluctuations introduce instabilities responsible, *e.g.* for the fragmentation of the system.

The self-consistent mean-field potential, U, is the one-body field generated by particles themselves. It is constructed using technique similar to those employed in Time-Dependent Hartee–Fock calculations [16]. Usually, a Skyrme parametrization is used [40] expressing the potential as a function of the nuclear matter density, ρ:

$$U(\rho) = \alpha\left(\frac{\rho}{\rho_o}\right) + \beta\left(\frac{\rho}{\rho_o}\right)^{\gamma}, \tag{2.7}$$

where $\rho_o = 0.17\,\mathrm{fm}^{-3}$, is the normal nuclear matter density, and α, β, and γ are the potential parameters. For given the values of ground-state nuclear matter density and binding energy per nucleon, the parameters α, β, and γ can be expressed as functions of nuclear matter compressibility parameter, K, only [41]:

$$K \equiv 9\rho^2\left(\frac{\partial^2 E/A}{\partial\rho^2}\right)_{\rho=\rho_o}, \tag{2.8}$$

using condition for the value of nuclear matter binding energy per nucleon ($E/A|_{\rho=\rho_o} = -15.48$ MeV), and the stationary condition at saturation point: $((\partial E/A)/\partial\rho)_{\rho=\rho_o} = 0$.

As a result of time evolution of the colliding system one obtains the matter density distribution:

$$\rho(\vec{r},t) = \int f(\vec{r},\vec{p},t)d^3p\,, \tag{2.9}$$

and the density distribution in momentum space:

$$g(\vec{p},t) = \int f(\vec{r},\vec{p},t)d^3r\,. \tag{2.10}$$

Before simulating the course of collisions, the ground state configuration of the colliding nuclei has to be calculated. Since ground state is a state with the minimum energy, the system energy minimization process is applied by enhancing the fermionic properties of the system.

The way of preparing the ground state configuration is different for BUU/VUU and BNV approximations. Unlike in the BNV approach, a collision term is included during preparation of the ground state configuration in the BUU/VUU. Exclusion of collision term is equivalent to solving the Vlasov equation.

There are different practical (numerical) techniques for solving the nuclear Bolzmann equation. One of the most common approaches is a test-particle technique. In this method, a large number of test-particles is used to represent each nucleon, with accordingly reduced interacting cross-section. This allows one to obtain a good coverage of phase-space. Another possibility is a parallel-ensemble method, in which many individual ensembles for each nucleon are calculated parallel in a common mean-field. After each step, an averaging over individual ensembles is performed. Such techniques have a common drawback. The system evolution is averaged during the calculations. In consequence, fluctuations and particle–particle correlations may be underestimated. Nevertheless, one can introduce quantum-statistical fluctuations by applying the Bolzmann–Langevin method [20]. The fluctuation term is acting as a source of density irregularities amplified by the self-consistent mean field. This effect reproduces system fragmentation and dynamical clusterization processes.

2.1.3. Molecular dynamics models

The molecular dynamics models developed for heavy-ion collision studies were adopted from chemical problems. They use classical equation of motion (see Eq. (2.2)) to describe the evolution of the system. The Classical Molecular Dynamics models (CMD) [21] neglect quantum effects describing, in consequence, the dynamics of *nucleons*, while the Quantum Molecular Dynamics(QMD) [23–25], and Quasi Particle Dynamics models (QPD) [26] are describing the evolution of *wave packets* associated with nucleons (quasi-particles). The QMD/QPD models simulate also such quantum-effects as Pauli-blocking. As in BUU/VUU models, collisions are blocked when the final phase-space states are occupied. The important difference is that the QMD/QPD approach takes into account individual, not averaged, collisions. In this manner the particle–particle correlations are introduced.

The exact treatment of Pauli principle requires significant computational time. This problem has found an interesting solution in the Constrained Molecular Dynamics Model (CoMD) [22], where the problem of the violation of Pauli principle was solved by adding a stochastic process to the usual QMD treatment.

In the QMD/QPD approach [23], nucleons (or quasi-particles) are represented by Gaussian minimal wave packets with a constant width:

$$\psi_i(\vec{r},t) = \frac{1}{(2\pi L)^{3/4}} e^{-\frac{(\vec{r}-\langle\vec{r}_i(t)\rangle)^2}{4L}} e^{-\frac{i}{\hbar}\langle\vec{p}_i(t)\rangle\vec{r}}\,, \tag{2.11}$$

where $\langle\vec{r}_i(t)\rangle$ and $\langle\vec{p}_i(t)\rangle$ are the mean position and momentum of the i-th nucleon, for a given time t, and L is the packet width.

The n-body wave function of a nucleus is then represented by a direct product of single particle functions ψ_i. As in the mean-field approximation, the quantum-mechanical analogue of n-body phase-space density distribution function is represented by a Wigner transform. For wave packets represented by Eq. (2.11) the n-particles reduced distribution function takes a form:

$$f(\vec{r},\vec{p},t) = \frac{1}{(\pi\hbar)^3} \sum_{i=1}^{n} e^{-\frac{1}{2L}(\vec{r}-\langle\vec{r}_i(t)\rangle)^2} e^{-\frac{2L}{\hbar^2}(\vec{p}-\langle\vec{p}_i(t)\rangle)^2}\,, \tag{2.12}$$

which describes the phase-space density at point $(\vec{r},\vec{p})$.

The time evolution of the system (n-body wave function) is assumed to be governed by the Ritz variational principle [23], what is equivalent to solving the classical Hamiltonian equations of motion (see Eq. (2.2)) for centroids of the Gaussian wave packets. Here the Hamiltonian has a form:

$$H = \sum_{i=1}^{n} \frac{\langle p_i^2\rangle}{2m} + U_{\rm nucl} + U_{\rm P} + U_{\rm C}\,, \tag{2.13}$$

where $U_{\rm nucl}$, $U_{\rm P}$, $U_{\rm C}$ are the nuclear, Pauli, and Coulomb potentials, respectively.

Using the Skyrme parameterization, the isospin-dependent nuclear potential energy density, $V_{\rm nucl}$ ($U_{\rm nucl} = \int V_{\rm nucl} d^3r$), can be expressed as:

$$\begin{aligned} V_{\rm nucl} \;=\; & \frac{\alpha}{2}\frac{\rho^2}{\rho_o} + \frac{\beta}{\gamma+1}\frac{\rho^{\gamma+1}}{\rho_o^{\gamma}} + \frac{C(\rho)}{2}\frac{(\rho_n-\rho_p)^2}{\rho_o} \\ & + \frac{G}{2}(\nabla\rho)^2 - \frac{G'}{2}\Big(\nabla(\rho_n-\rho_p)\Big)^2\,, \end{aligned} \tag{2.14}$$

where $\rho_o = 0.17\,{\rm fm}^{-3}$, is the normal nuclear matter density, and ρ_p and ρ_n are proton and neutron densities, respectively. The potential parameters α, β, and γ are related to the nuclear matter compressibility parameter K — see Eq. (2.8). The symmetry energy term parameter, $C(\rho)$, is related to the nuclear matter isospin asymmetry. With different parameterizations of the symmetry term coefficient, C, one can obtain the ASY-STIFF EOS: $C = 31.4\,{\rm MeV}$, or the ASY-SOFT EOS: $C = 76.5{-}45.1(\rho/\rho_o)$ MeV [42]. The last two terms in Eq. (2.14) correspond to isoscalar and isovector components of the symmetry energy, respectively.

By taking the n-body wave function as a direct product of single particle functions, one violates the Pauli principle. Nevertheless, the antisymmetrization effects can be simulated by a Pauli potential acting between particles of the same kind, *i.e.* having the same isospin and spin:

$$U_p = \frac{1}{2} V_o^p \frac{\hbar^2}{16mL^2} \sum_{i=1}^{n} \sum_{j \neq i}^{n} \frac{Q_{ij}^2}{e^{Q_{ij}^2/4L} - 1}\,, \tag{2.15}$$

where V_o^p is a scaling factor, introduced to reproduce energetics of three- and higher-body systems and Q_{ij}^2 is a measure of the distance in the phase-space:

$$Q_{ij}^2 = (\langle \vec{r}_i \rangle - \langle \vec{r}_j \rangle)^2 + \frac{4L^2}{\hbar^2} (\langle \vec{p}_i \rangle - \langle \vec{p}_j \rangle)^2 \,. \tag{2.16}$$

By inspecting formulas (2.15) and (2.16) one can find that the Pauli potential, simulating the Pauli principle, prevents nucleons of the same kind being too close in the phase space.

As in the mean-field approximation, ground states of the colliding nuclei are calculated. Mathematically, the ground state configuration is equivalent to phase space configuration minimizing the system Hamiltonian. It is the way of preparing of the ground state configuration which differs the QMD and QPD approach [23, 26]. The latter time evolution of the system is calculated assuming that the mean positions and momenta of N nucleons are evolving in the effective potential, taking into account two-body effective nucleon–nucleon interactions along classical trajectories. The scattering of nucleons is related to the nucleon–nucleon cross-section, σ_{NN}, which is energy and isospin dependent [43]. Any two nucleons become candidates for collision, if their spatial distance, r_{ij}, is less than the distance determined by the nucleon–nucleon cross-section:

$$r_{ij} < \sqrt{\frac{\sigma_{\mathrm{NN}}}{\pi}}\,. \tag{2.17}$$

The collisions take place if the final states are not occupied by nucleons of the same kind (Pauli blocking). The Pauli potential together with Pauli blocking simulates the Pauli principle for n-body wave function taken as direct product of single particle functions (Eq. (2.12)).

The time evolution of the system is calculated within certain time interval, which is a model parameter (usually 300 fm/c). When the dynamical evolution is stopped, the clusters are identified. In the CHIMERA QMD code [44], results of which are presented here, the proximity in the configuration space is used for cluster definition. Thus, it is assumed that nucleons form a cluster when the distance between them is less then 3 fm. For each

cluster, the charge, mass, position, momentum, spin, and excitation energy is determined.

A simulation of the Pauli principle, which is a common drawback of the QMD/QPD approach, was improved in the fermionic molecular dynamics (FMD) models [28], which represents a true quantum treatment of the n-body wave function. In the FMD approach the n-body state is taken as an antisymmetrized Slater determinant. The FMD dynamics is fully deterministic, and the system wave function remains a Slater determinant at all times.

The drawback of deterministic character of FMD is not present in the antisymmetrized molecular dynamics (AMD) models [27]. Here, stochastic terms are added to equations of motion, which properly treat the fluctuations in reaction dynamics.

2.2. Deexcitation models

As the collision models give information about the properties of primary excited fragments, formed in the early collision stage, the final deexcitation is calculated by deexcitation models. Here, we present the description of *statistical* deexcitation models, as we focus on dynamical and statistical aspects of fragment emission. The presented statistical models are usually used as "afterburners" in any two-stage reaction modeling.

2.2.1. Sequential statistical emission models

The sequential statistical emission models treat deexcitation of hot fragments as a chain of statistically independent decays. The computer codes like GEMINI [45], BINFRA [46] or SIMON [47], are based on the transition-state method [37,38] which treats the evaporation of particles and fission as different modes of the same decay mechanism.

Assuming the Fermi-gas level densities, the probability of decay of a nucleus of mass A at an excitation energy E^* into two daughter nuclei A_i and A_j, can be expressed as:

$$P(A; A_i, A_j) \propto \frac{e^{2[a(E^* - E_{\rm sep} - E_{\rm C} - E_{\rm rot} - 2T)]^{\frac{1}{2}}}}{e^{2[aE^*]^{\frac{1}{2}}}}\,, \tag{2.18}$$

where $E_{\rm sep}$, $E_{\rm C}$, $E_{\rm rot}$, and T are the ground-state separation energy, the Coulomb barrier and the rotational energy, and the temperature at the saddle-point, respectively.

The temperature T is evaluated using the relation between excitation energy and temperature for a compound nucleus:

$$E^* = aT^2\,, \tag{2.19}$$

where a is the level density parameter. In the formula (2.18) the factor $2T$ in the upper exponent is responsible for the fluctuations at the saddle-point transition.

According to transition-state method, the corresponding decay widths are calculated taking into account all possible modes of decay:

$$\Gamma_{\rm TSM} = \frac{1}{2\pi\rho} \int\limits_0^{E^*-E_{\rm sad}(J)} \rho_{\rm sad}(U_{\rm sad}, J) dE\,, \tag{2.20}$$

where ρ and $\rho_{\rm sad}$ are the level density of initial system, and the saddle point configuration, respectively. $U_{\rm sad}$ and $E_{\rm sad}(J)$ are the thermal excitation energy, and the deformation plus rotational energy, at the saddle point, respectively. Here, E is the kinetic energy of the transitional degree of freedom.

Although the transition state method can be used to calculate all possible decays, from neutron and proton evaporation to symmetric fission, more precise approach can be obtained using the Hauser–Feschbach formalism [48]. In this case, the decay width for emission of a particle (Z_1, A_1) having spin J_1, from a parent nucleus (Z, A) having spin J and excitation energy E^*, leaving the residual nucleus (Z_2, A_2) is:

$$\Gamma_{\rm HF} = \frac{2J_1+1}{2\pi\rho} \sum_{J_2} \sum_{l=|J-J_2|}^{J+J_2} \int\limits_0^{E^*-B-E_{\rm rot}(J_2)} T_l(E)\rho_2(U_2, J_2)\, dE\,, \tag{2.21}$$

where ρ and ρ_2 are the level density of initial, and residual systems, respectively. Here, l denotes the orbital angular momentum, and J_2 the spin of the residual system. $E_{\rm rot}(J_2)$ is rotation plus deformation energy of the residual system, and B is the binding energy. The integration is performed over the kinetic energy of emitted particle, E, taking into account the transmission coefficient $T_l(E)$.

The Hauser–Feshbach formalism can be derived from Weisskopf emission rates [49]:

$$\Gamma_{\rm Weisskopf} = \sum_{i=1}^{n} \int\limits_0^{E^*-B-\varepsilon_i^*} (2s_i+1)\frac{\mu}{\pi^2\hbar^3}\sigma_{\rm inv}(E)\,\frac{\rho(E^*-B-E)}{\rho(E^*)} E\, dE\,, \tag{2.22}$$

where E is the kinetic energy of emitted particles, μ is the reduced mass, and ε_i^* denotes the ground and all excited states of emitted particle.

The Weisskopf formalism requires the knowledge of cross-section, $\sigma_{\rm inv}(E)$, for the inverse (fusion) reaction, which can be calculated using *e.g.* the optical model.

Since the Hauser–Feschbach formalism is more complicated, as compared to the transition-state method, and requires more computing time, its application in the GEMINI code was limited to emission of fragments with $Z \leq 3$. In the BINFRA code, the transition-state method is used for emission of all particles. Alternatively, the SIMON code uses Weisskopf emission rates.

During the sequential decay calculations, the consecutive binary decays of the initial hot nucleus are calculated until all decay fragments become "cold". Here, as a "cold" we assume a fragment with an excitation energy below the yrast line, *i.e.* no more particle emission is possible. After each binary partition, the charge, mass, excitation energy, and spin of the daughter fragments are calculated.

The sequential emission models differ mainly by the evaporation formalism (transition-state, Hauser–Feshbach, or Weisskopf method), and by approximations used to calculate the emission barriers, and the separation and rotational energy (see Eq. (2.18)).

2.2.2. Prompt statistical emission models

The idea of a prompt (simultaneous) break-up of hot nucleus into many fragments was introduced by Randrup and Koonin in 1981 [50]. Since then, many multifragmentation models were proposed, based on microcanonical, canonical, macrocanonical, or grand canonical ensembles [9, 51, 52]. The prompt break-up is expected to produce hot fragments, so a subsequent sequential deexcitation of hot fragments should also be included [52].

The multifragmentation process can be classified according to the final set of fragment multiplicities, called the break-up partition:

$$f = \{N_{AZ};\, 1{\leq}A{\leq}A_o,\, 0{\leq}Z{\leq}Z_o\}\,, \tag{2.23}$$

where A_o and Z_o are the mass and charge of breaking system.

The multifragmentation models calculate the break-up partitions (events) according to assumed statistical ensembles. Here, a statistical ensemble is a complete (or limited) set of channels, f, satisfying the conservation laws for mass, charge, energy, momentum, and angular momentum of the decaying system, characterized by statistical weights $\Delta\Gamma_f$.

The exact way of all partition treatment is given by the microcanonical ensemble, in which, by definition, all microscopic states of the system obey strictly conservation laws. However, using the microcanonical ensemble presents very complicated numerical problem. In fact, it was not applied in multifragmentation models in a full scale. To some extent it was used in the Microcanonical Metropolis Monte Carlo code (MMMC) [9].

Using microcanonical ensemble, one encounters problems with sampling of the possible partition space. Thus, for example the number of possible multifragmentation partitions is 1.9×10^8 for a system with mass 100, and 3.9×10^{12} for a system with mass 200. One of the possible solutions is a Metropolis method [53]. This method is based on an observation that the available phase-space is not populated uniformly, usually showing sharp peaks in the process probability distribution. The main issue of Metropolis sampling is finding these regions. For this purpose a Markovian sequence of partitions, $\{f\}$, is generated. The sequence starts with a given partition, f, with weight $\Delta\Gamma_f$, for which a trial partition, $f^{'}$, with weight $\Delta\Gamma_{f'}$, is generated, using "small" steps in the partition space. If $\Delta\Gamma_{f'} > \Delta\Gamma_f$, a new partition is included into the partition set. Otherwise it is included with weighted probability $\Delta\Gamma_{f'}/\Delta\Gamma_f$. Such procedure is repeated for different available phase-space directions, until the representative set of partitions is found. This approach has two drawbacks: *(i)* some important physical processes with small probabilities are rejected; *(ii)* if the model approximations are not precise, the Metropolis method could produce artifacts, *i.e.* partitions with probabilities too small to be ever produced in nature (note that process probabilities have exponential forms).

A different approach to partition space sampling is used in the Statistical Multifragmentation Model (SMM) [52]. The SMM approach is based on a hybrid method combining canonical and macrocanonical ensembles. The algorithm starts with mass and charge distributions, $\langle N_{AZ}\rangle$ and $\langle N_A\rangle$, calculated analytically using macrocanonical ensemble. It is based on variational method, assuring that the mass and charge distributions are proportional to probability of finding a fragment (A, Z) in the sampled ensemble. Subsequently, the following algorithm sequence is applied: *(i)* the temperature and chemical potentials determining $\langle N_{AZ}\rangle$, $\langle N_A\rangle$, and consequently $N_A(Z)$ distributions are found; *(ii)* the fragment mass is randomly chosen according to the $\langle N_A\rangle$ distribution; *(iii)* the fragment charge is determined according to $N_A(Z)$ distribution; *(iv)* such procedure is repeated until mass and charge conservation rules are satisfied. In consequence, this method selects partitions which are close to the most probable ones.

When a partition is selected, fragment excitation energies and momenta are calculated. By solving the microcanonical equation of energy balance, the temperature for a given partition, T_f, is calculated. Knowing the temperature, the average excitation of fragments is calculated assuming equipartition of energy. The momenta are calculated assuming Maxwell–Bolzmann distribution for a given temperature T_f.

Due to high excitation energy (pressure), the nuclear matter will expand, until the break-up configuration is reached. The break-up configuration in the SMM model is associated with a thermal bath (thermostat). Therefore, excited fragments are having the same temperature.

The fragments positions in the initial configuration are chosen randomly, assuring non-overlapping configuration. If necessary, the fragments momenta are scaled in order to obey conservation rules. The break-up (freeze-out) volume, V, is given by the model parameter κ:

$$V = (1 + \kappa)V_{\rm o}\,, \tag{2.24}$$

where $V_{\rm o}$ denotes the volume of the original cold nucleus of mass A, and charge Z. The κ parameter is equal 2 in the original version of the model [52] (see discussion about break-up volume in the next chapter). By definition, the freeze-out volume is a break-up configuration in which fragments are separated, interacting only via Coulomb forces.

After assigning fragments positions, the partition is propagated under the mutual Coulomb forces starting from the break-up configuration. The final fragment deexcitation is calculated assuming a binary sequential decay scenario with decay rates given by the Weisskopf approximation — see Eq. (2.22). Additionally, the SMM model assumes the possibility of Fermi break-up of excited fragments [52]. This mechanism is limited to light fragments ($A \leq 16$) with relatively small excitation energy, comparable with a total binding energy. In this case an explosive decay of excited fragments into smaller clusters is performed.

As an alternative to existing prompt multifragmentation models, one can consider the Expanding Emitting Source model (EES) [54]. Here, a very short time-scale emission is connected with the expansion phase. It is based on an extended Weisskopf evaporation model, coupling the emission rates with decay volume and source entropy.

2.2.3. The MULFRA model

The prompt multifragmentation MULFRA model [55, 56] was devoted to study kinematical differences between prompt and sequential decays. It uses partitions generated by sequential decay codes [45, 46]. The generated partitions are placed in the break-up (freeze-out) volume and propagated subject to mutual Coulomb interactions.

The idea of using the same partitions in both, prompt and sequential decay, came from the study of experimental data, especially the fragment size distributions (charge or mass spectra). The existing decay codes are predicting similar final charge and mass spectra for a wide range of bombarding energies [57]. Therefore, it is impossible to distinguish between different decay scenarios by simply comparing fragment size distributions. On the other hand, the same partitions with different velocity distribution will give different picture when an emulator of the experimental set-up is used. This is because the detectors positions and thresholds are modifying the initial distributions, according to fragment velocity (energy) distributions.

In distinction between different decay scenarios, the crucial role is played by the emission time-scales. A fast chain of sequential binary decays will result in similar effects as a prompt break-up [56]. In fact, the theoretical and experimental esitimations [58] predict nuclear lifetimes of an order of 10^{-18} to 10^{-23} s, for temperatures increasing from 1 to 10 MeV, respectively. It means, that for high excitation energies, the difference between prompt and sequential scenarios is small from the point of view of nuclear life-times.

The above considerations provided a motivation for developing the code MULFRA, using the same partitions as produced by sequential decay codes. Taking into account, that the prompt break-up is expected to produce hot fragments [52], the partitions generated by BINFRA [46] or GEMINI [45] codes are stopped at some level of fragments average excitation energy, *e.g.* 20% of total excitation energy per nucleon [56].

The prompt break-up simulation starts with constructing the initial break-up configuration based on the partition produced by one of binary sequential codes. For this purpose, the $3N$ configuration space minimization maximum-packing algorithm is used, ensuring a configuration of non-overlapping spheres. The break-up (freeze-out) volume distribution, resulting from applied algorithm is presented in Fig. 1.

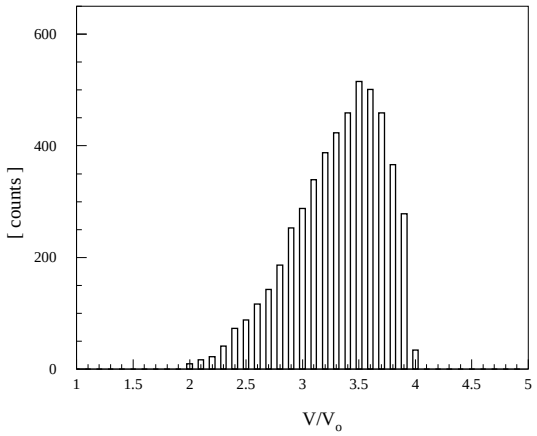

Fig. 1. Distribution of freeze-out volume, V, normalized to the volume V_o of a normal nucleus (here ^{150}Sm).

The distribution presented in Fig. 1 is quite broad, having its maximum about $3.5\times V_{\rm o}$. In contrast to other multifragmentation codes, the freeze-out volume is here not a model parameter, but a result of applied maximum packing algorithm. In the SMM code [52] the freeze-out volume is $3\times V_{\rm o}$ (see Eq. (2.24)), and in the MMMC code [9] $6\times V_{\rm o}$. The initial freeze-out configuration plays important role in the system energy balance, defining the

Coulomb energy, $V_{\rm C}$. The larger is the freeze-out volume, the smaller is the system Coulomb energy. Consequently, the larger amount of the available energy can be assigned to fragments thermal and collective degrees of freedom, according to total energy conservation. This has a significant impact on calculated reaction dynamics. Moreover, it is not realistic to expect that the prompt break-up will occur in fixed value of freeze-out volume. One should rather expect some freeze-out volume distribution, especially that the freeze-out configuration is a function of the fragment partition, *i.e.*, will be different for symmetric and asymmetric mass partition [56].

Having defined the spatial break-up configuration, the available kinetic energy, $K = E^{\rm tot} - V_{\rm C}$, is distributed by assigning the initial velocities to all fragments [56]. Later on, the fragment velocities are re-normalized in order to obey the energy, total linear-momentum, and total angular-momentum conservation laws.

After defining the spatial configuration and velocity distributions, the break-up configuration is fully described. At this point the system disintegrates and the fragments are accelerated in the mutual Coulomb field. The fragments equations of motion are integrated numerically.

The fragments can be excited, decaying in-flight with proper decay constants (see next chapter). For this purpose one of the sequential binary codes is used.

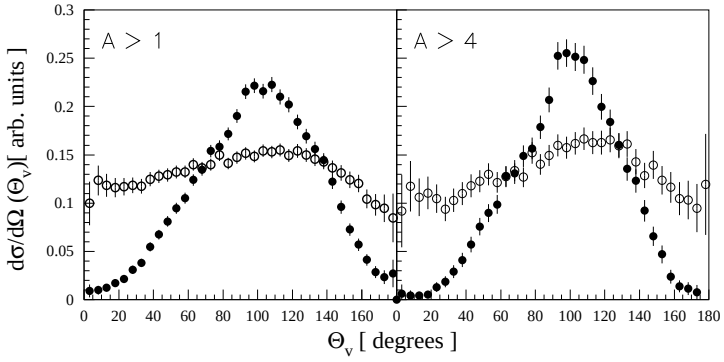

Fig. 2. Angular distribution of fragment velocity vectors ($A > 1$ and $A > 4$) for the sequential binary decay — open circles, and for the prompt multifragmentation — close circles.

The kinematical differences between sequential and prompt alternatives are well illustrated in Fig. 2, where the distributions of fragment velocities (excluding the two heaviest ones), are shown in the center-of-mass (c.m.) frame with v_x axis defined by the relative velocity of two heaviest fragments $(\vec{v}_1 - \vec{v}_2)$. Here, θ_v is the angle between the v_x axis and the fragment velocity vector. This angular distribution of velocity vectors is a Gaussian-like curve

for the prompt break-up, while for a sequential break-up it is a more isotropic one. Such a strong Coulomb focusing effect for prompt multifragmentation scenario is connected with influence of the Coulomb field created by the two heaviest fragments.

2.2.4. Dynamical versions of sequential emission models

The sequential emission models like GEMINI [45], BINFRA [46] or SIMON [47] are static, *i.e.* they do not include fragments dynamics. The decaying fragments are obtaining their Coulomb asymptotical velocities after each break-up. This means that no decay time scales are included, and there is no proximity effect of other decaying fragments.

In order to introduce dynamics one has to evaluate lifetimes of the excited nuclei. These lifetimes depend on the emission mode. Assuming the correctness of the transition-state method [37, 38], light fragment evaporation, IMF emission, and fission, can be treated as different cases of the same decay mode. Therefore, a common nuclear lifetime parameterization, based on theoretical estimations [58] was proposed [56]:

$$\tau = 2e^{13/T}e^{A/8}\,[\mathrm{fm}/c]\,, \tag{2.25}$$

where T [MeV] is nuclear temperature, and A is the mass of the emitted fragment. Such a parametrization is used in the dynamical version of the BINFRA code [56].

Another possibility is using the Heisenberg principle. In this case the nuclear lifetimes are given by the decay-width:

$$\tau = \frac{\hbar}{\Gamma_{\mathrm{tot}}}\,, \tag{2.26}$$

where Γ_{tot} is the total decay width, including all decay channels. This method was used in the dynamical version of the GEMINI code [59].

The main difference between parameterized lifetimes and lifetimes defined by decay-widths is the model consistency. The decay-width gives the description of decay modes, which are, of course, dependent on details of the applied model. Therefore, the decay lifetimes as given by formula (2.26) are related directly to model approximations. Moreover, by comparing formulas (2.25) and (2.26) one can find that the formula (2.25) does not include explicit dependence on mass of the decaying system, as it was constructed using data from different reactions [58] (note the implicit dependence on the nuclear temperature).

The dynamic simulation of sequential binary decay is performed by integrating equations of motion for all fragments between the successive decays. The decay times are generated using formula (2.25) in BINFRA code [56],

or formula (2.26) in GEMINI code [59]. The static versions of BINFRA [46] or GEMINI [45] codes are using Coulomb asymptotical velocities, what excludes the interaction via Coulomb forces between the fragments.

For the evaluation of decay time scales, and dynamics of fragments in the mutual Coulomb field, the correlation function between pairs of charged fragments can be used. Here we use the $1 + R$ correlation function of the reduced velocity, $v_{\rm red}$, between pairs of fragments with a charge Z_i and Z_j, respectively:

$$1 + R \equiv \frac{N_{ij}^{\rm true}(v_{\rm red})}{N_{ij}^{\rm mix}(v_{\rm red})}\,, \tag{2.27}$$

with the reduced velocity, $v_{\rm red}$, defined as:

$$v_{\rm red}{=}\frac{v_{\rm rel}}{\sqrt{Z_i + Z_j}}\,, \tag{2.28}$$

where, $v_{\rm rel}$ denotes the relative velocity, $N_{ij}^{\rm true}$ is the true number of correlations between pairs of fragments, and $N_{ij}^{\rm mix}$ is the number of random correlations (here six subsequent events were mixed).

The reduced velocity correlations for decay of the ^{70}Se nucleus excited to 520 MeV, as predicted by the static and dynamical versions of the GEMINI code, are presented in Fig. 3. The $1{+}R$ distribution shows a big difference for small values of $v_{\rm red}$, where the emitted fragments are expected to be closer in space and in time, interacting via the Coulomb forces. The reduction of the correlation function ("the Coulomb hole") for small values of the reduced velocity is not reproduced by the GEMINI code without time scales. This is because all subsequent decays are independent, and the emitted fragments

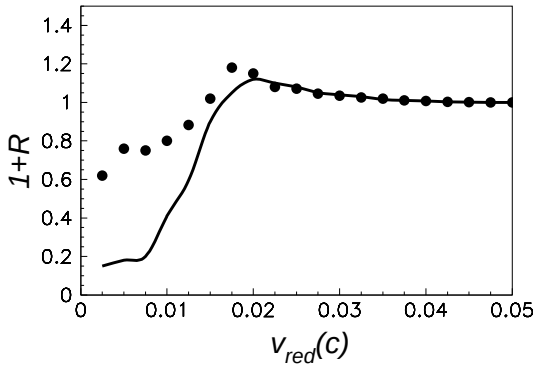

Fig. 3. Reduced velocity correlations for particles with $2 \le Z \le 6$. Calculations were performed with the GEMINI code with no time-scales (black circles) and with time-scales calculated from decay widths (solid line).

do not interact via Coulomb forces. The inclusion of dynamics, and consequently, the Coulomb repulsion between close fragments can dramatically change the behavior of observables based on fragment velocity distributions.

3. Experimental set-ups and procedures

Since many years the 4π multidetector systems were in wide use in heavy-ions collisions study. In the past two decades a huge progress was made in improving the detection efficiency, mainly by increasing the number of detectors, and lowering the detection thresholds. Thus, *e.g.* while the AMPHORA [60] and DWARF BALL/WALL [61] systems, were consisting of 139 and 105 detectors, respectively, the INDRA [62] multidetector has 336 detectors. The most sophisticated multidetector array CHIMERA [63], used for the studies of heavy-ion collisions at intermediate energies, has 1192 detectors.

The development of 4π multidetector arrays was aimed not only at increasing the detection granularity but much effort was also devoted to lowering the detection thresholds. The ionization chambers installed in the INDRA multidetector have significantly lowered the detection thresholds, especially for intermediate-mass fragments. Different solution was used in the CHIMERA multidetector. Here, the time-of-flight (TOF) technique was used to identify particles stopped in the Si element of the Si-CsI(Tl) telescopes. Such a solution has drastically lowered the detection thresholds for all particles.

Even the most sophisticated charged-particle multidetector will always miss information about the emitted neutrons. This fact has a definite impact on event reconstruction, and disallows to study correlations between emitted neutrons and charged particles. This situation provided a motivation to simultaneous measuring of neutrons and charged particles in a 4π configuration. The idea has been realized in the full scale by using the Rochester RedBall [64] calorimeter together with the Dwarf Ball/Wall multidetector [5, 6]. The neutron detection has been later improved by constructing the Rochester SuperBall calorimeter [65]. This has increased the detection efficiency from $\varepsilon \approx 0.5$–0.6 for RedBall, to $\varepsilon \approx 0.82$ for the SuperBall detector.

3.1. The charged-particle detector arrays

In the following chapters two 4π experimental set-ups are described: *(i)* The AMPHORA multidetector used in the ^{40}Ca+^{40}Ca experiment at 35 MeV/nucleon; *(ii)* The DWARF BALL/WALL multidetector used in the ^{136}Xe+^{209}Bi experiments at 28, 40, and 62 MeV/nucleon, together with the Rochester RedBall/SuperBall neutron calorimeters.

3.1.1. The AMPHORA multidetector

The AMPHORA 4π system [60] was designed at ISN Grenoble for heavy-ion collision studies. It consists of the BALL and the WALL parts, including a total of 139 CsI(Tl) detectors. The WALL part consists of 48 hexagonal phoswitch detectors, with 200 μm thick plastic scintillator, optically connected to CsI(Tl) crystals. The BALL part consists of 91 detectors: *(i)* 15 phoswich detectors with 100 μm thick plastic scintillator at polar angle $\Theta_c = 20°$, *(ii)* 30 ionization chambers [66] and CsI(Tl) crystals, placed at $\Theta_c = 31°$ and $\Theta_c = 47°$, and *(iii)* 47 CsI(Tl) detectors placed in Θ_c range between 67° and 148° (Θ_c refers to the center of the detector).

The implementation of ionization chambers, presenting an improvement, as compared to standard AMPHORA configuration, resulted in lowering the thresholds for intermediate-mass fragment detection from 5–7 MeV/nucleon to about 1 MeV/nucleon [66].

The particle identification was carried out using pulse-shape technique, for phoswich detectors and CsI(Tl) crystals. The light charged particles ($Z \leq 2$) were identified with isotopic resolution. For heavier fragments ($3 \leq Z \leq 25$), a good charge resolution was obtained. In the ^{40}Ca+^{40}Ca experiment at 35 MeV/nucleon, the energy calibration was made using calibration beams of ^{4}He, ^{12}C, ^{16}O, and ^{20}Ne, for four different energies.

In order to minimize random coincidences ("pile-up" events), the low beam intensity, together with no on-line multiplicity trigger, was used in the ^{40}Ca+^{40}Ca experiment. This allowed to acquire events over the large range of impact parameters.

By using the on-line multiplicity trigger one "cuts-off" the very peripheral collisions, in which the charged-particle emission is small. Note that for very low excitation energies (very peripheral collisions), the fragment deexcitation proceeds mainly via neutron emission. Therefore, the charged particles detector arrays are missing substantial fraction of the reaction cross-section, due to the insensitivity of the event trigger to neutrons.

3.1.2. The DWARF BALL/WALL multidetector array

The Dwarf BALL/WALL multidetector [61] was built at Washington University in St. Louis. It consists of a Wall section with 40 CsI(Tl) plastic scintillator phoswiches and of the Ball part with 65 CsI(Tl) plastic scintillator phoswiches — see Fig. 4. The Dwarf Wall is covering an angular range from 4° to 32°, and the Dwarf Ball the range from 32° to 168°. At forward angles the plastic scintillators have thicknesses varying from 60 to 175 μm. At angles larger than 40°, the thickness of plastic scintillators is from 10 to 30 μm. The front of the plastic scintillators is covered with a 150 μg/cm^2 aluminized Mylar foil. The four most forward Dwarf Wall detectors are additionally shielded with ≈ 200 mg/cm^2 Pb absorbers.

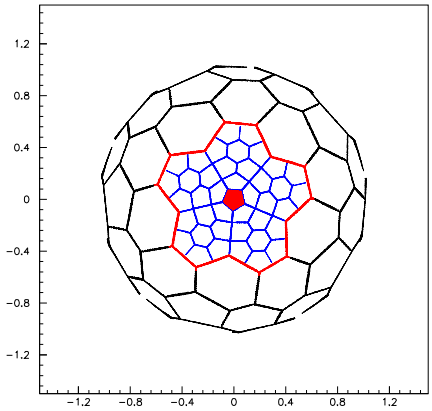

Fig. 4. The schematic view of the DWARF BALL/WALL 4π multidetector array. The "Dwarf-Wall" part in the middle (high detectors granularity) is surrounded by the "Dwarf-Ball". The beam entry is in the back. The solid angle coverage is about 82% ($4^\circ \leq \Theta \leq 168^\circ$).

The Dwarf BALL/WALL multidetector system is operating using pulse-shape discrimination technique. Three integration gates, one covering the fast plastic scintillator pulse, and two covering the slow CsI(Tl) pulse, are used for particle identification and energy calibration. A good isotopic light charged particle ($Z \leq 2$) identification can be obtained. The charge identification is very good for $3 \leq Z \leq 16$, and still fairly good for $17 \leq Z \leq 40$.

Because of the finite thickness of the fast plastic scintillator, the Dwarf Ball/Wall array has a rather high detection thresholds for intermediate-mass and heavy fragments, especially for the WALL section. The average detection thresholds are shown in Fig. 5. The average efficiencies for the

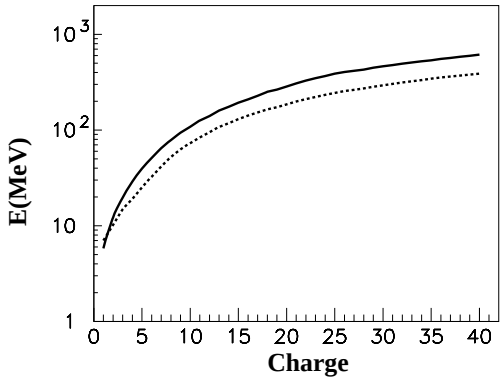

Fig. 5. Average detection thresholds for DwarfWall (solid line) and DwarfBall (broken line) detector arrays.

entire Dwarf BALL/WALL detector for light-charged particles (LCP) and intermediate-mass fragments (IMF) detection are shown in Table I.

TABLE I

Average efficiency for LCP, and IMF($3 \leq Z_{\rm IMF} \leq 16$) detection for ^{136}Xe+^{209}Bi reactions at $E/A = 28$, 40 and 62 MeV, respectively.

SPECIES	28 MeV/nucleon	40 MeV/nucleon	62 MeV/nucleon
LCP	0.42	0.38	0.32
IMF	0.38	0.32	0.25

In the ^{136}Xe+^{209}Bi experiments, eight small-angle DwarfWall detectors were removed and replaced by position-sensitive silicon-detectors for the detection of projectile-like fragment. The latter were placed at very forward angles, including the angular region close to the grazing angle ($\theta = 4.48°$, 3.90°, and 2.91°, for 28, 40, and 62 MeV/nucleon reactions, respectively). One of the DwarfBall detectors was removed to accommodate the target mechanics. Additionally, in the 40 and 62 MeV/nucleon experiments, four of the Dwarf Ball phoswitch detectors were replaced by two Si–Si and two Si–CsI detectors allowing mass resolution up to $Z = 8$.

The Dwarf BALL/WALL detectors were placed inside the hollow center of RedBall/SuperBall neutron multiplicity meters. The latter have inherently long dead times resulting from their principle of operation and, therefore, the combined RedBall/Superball and Dwarf BALL/WALL 4π detector systems were used with low beam intensities (few hundred counts per second maximum) ensuring low rate of event pile-ups.

3.1.3. Charged-particle detectors calibration

The charged-particle detector calibration is usually done in two steps: *(i)* first, the particle identification is performed, *(ii)* then the energy calibration is done using detector signals for identified particles. In order to identify particles, at least two parameters are needed. These can be the raw detector signals, *e.g.* signals from two elements of the telescope detector, or detector signal and time-of-flight measurement signal. In this chapter we present calibration methods for phoswich detectors, although these methods can be adapted for calibrating other kinds of detectors.

The phoswich detectors are built from two scintillators of different time constants — a fast-plastic transmission scintillator and a thick ("stop") slow-response CsI(Tl) crystal. The two scintillators are optically coupled with each other and with a photomultipler tube to allow the latter to collect efficiently light from both of them. The operating principles for phoswich detectors are presented in Fig. 6.

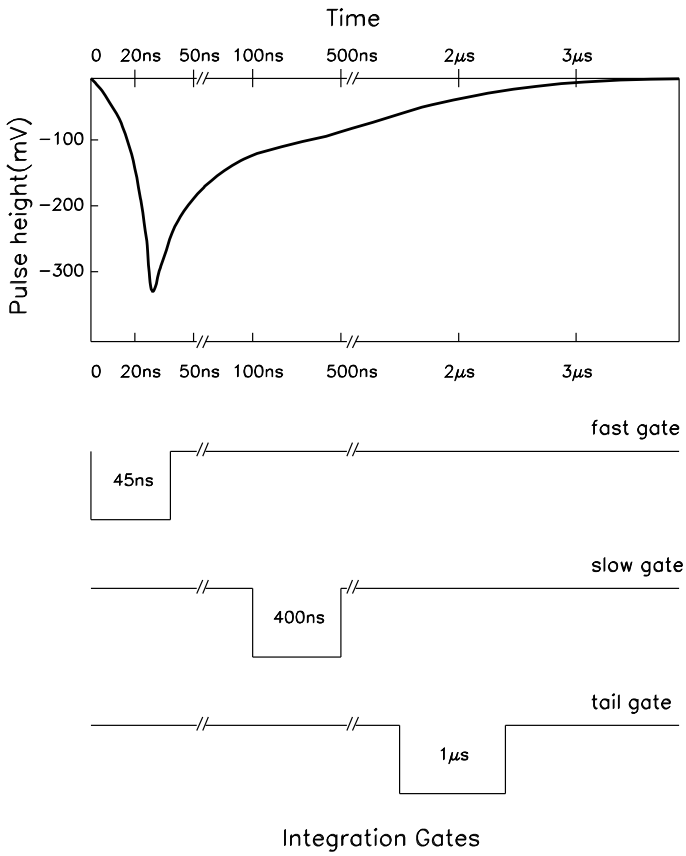

Fig. 6. The shape of a typical signal from a phoswich detector and the definition of the integration gates for "fast", "slow" and "tail" components of the light output signal [67].

The negative electronic pulses representing the detector responses to impinging particles are routed in parallel to three charge-integrating analog-to-digital converters, QDCs, set to integrate the charge within three different time-windows or slices. Fig. 6 indicates also the operational definition of the three QDC gating signals – "fast", "slow", and "tail". The gates are set so as to optimize separation of the three physical components of the composite light output signal from the fast-plastic and CsI(Tl) scintillators. The partial charge of the photomultiplier signal integrated within the "fast" gate represents dominantly the "fast" component contributed by the fast-plastic scintillator, while the partial charges integrated within the "slow" and "tail" gates are dominated by contributions by the "slow" and "tail" components in the CsI(Tl) light output, respectively.

It is clear from Fig. 6 that no choice of gating signals can provide for an ideal separation of the physical components of the composite signal, as these components overlap in time to a significant degree. For example, "fast" signal represents not only the energy lost by the particle in the fast plastic, but contains also a significant contribution from the light output generated in the CsI(Tl) crystal. Similarly, "slow" signal is contributed by light associated with energy deposited by the particle in the fast plastic scintillator, albeit to a lesser extent. Conversely, "tail" signal is contributed by the "slow" component of the composite signal.

The standard particle identification method used in charged particle detectors is based on constructing contour gates encompassing individual observed "ridges". Here we propose using identification functions, instead. In case of phoswich detectors, two families of functions were constructed [67], expressing the strength of the "fast" signal, F, as a function of the strength of the "slow" signal, S:

$$F = f(Z, S)\,, \tag{3.1}$$

where Z is the particle atomic number.

By expressing the identification curves as a function of particle charge, one obtains a parameterization which can be extrapolated to higher charges. This makes it possible to identify, albeit less reliably, especially for particles which are produced with low statistics. In fact, as it was shown in Ref. [67], the extrapolation of identification fit made for $3{\leq}Z{\leq}16$, gave a good charge identification up to $Z = 35$. The possibility of an extrapolation of particle identification is also important for the calibration of backward detectors, where because of the reaction kinematics, the statistics is usually small, especially for heavier fragments.

The formula (3.1) represents a specific case, which can be generalized for any type of telescope detector:

$$\Delta E = f(Z, E)\,, \tag{3.2}$$

where ΔE and E denote the signals in transmission, and stop detector elements, respectively. In the case of Si–Si or Si–CsI detectors, the identification functions are much simpler, because there is no signal mixing in this case.

The standard energy calibration procedure is based on reference energy obtained during measurement of elastic scattering of different heavy-ions beams [68]. For calibration of the CsI(Tl) crystals, one uses the relation between the deposited energy and the light output, with the latter approximated by the "slow" signal, S [67, 68]:

$$E_{\mathrm{csi}} = a_{\mathrm{csi}} w_{\mathrm{csi}} S + Z\, b_{\mathrm{csi}} \ln(1 + c_{\mathrm{csi}} w_{\mathrm{csi}} S)\,, \tag{3.3}$$

where $w_{\rm csi}$ is an overall light attenuation factor, and $a_{\rm csi}$, $b_{\rm csi}$, and $c_{\rm csi}$ are known coefficients [68]:

$$a_{\rm csi} = 0.1772\,, \qquad b_{\rm csi} = 16.46\,, \qquad c_{\rm csi} = 0.005213\,. \tag{3.4}$$

This method cannot be used for backward detectors, where the elastic scattering is not seen. Here we propose a new method, based entirely on relationship between the "fast" and "slow" signals [67]. The light output signals from plastic scintillator and CsI(Tl) crystals overlap, as mentioned earlier.

Because of the light output overlap, the observed intensities of the "fast" (F) and "slow" (S) parts of the composite detector response signal are related to the two physical (true) light output components, $F^{\rm r}$ and $S^{\rm r}$, via the linear transformations,

$$F = F^{\rm r} + Q^{\rm S}_{\rm mix} S^{\rm r}\,, \tag{3.5}$$

and

$$S = S^{\rm r} + Q^{\rm F}_{\rm mix} F^{\rm r}\,. \tag{3.6}$$

Here, $Q^{\rm S}_{\rm mix}$ and $Q^{\rm F}_{\rm mix}$ are the respective light output overlap constants.

The relation between the deposited energy and the light output for CsI(Tl) crystals ("slow" signal) is given by Eq. (3.3). It is reasonable to assume [67], that a similar relationship will be valid for plastic scintillators ("fast" signal), with parameters specific to the material (here: polyvinyltoluene):

$$E_{\rm pl} = a_{\rm pl} w_{\rm pl} F + b_{\rm pl}(Z) \ln(1 + c_{\rm pl} w_{\rm pl} F)\,, \tag{3.7}$$

where the quantity $w_{\rm pl}$ is a gain factor valid for a specific detector, while the parameters $a_{\rm pl}, b_{\rm pl}$, and $c_{\rm pl}$ describe the relationship between energy deposit and light output for polyvinyltoluene.

The new calibration method is based on simultaneous fit of functions describing the dependence between the light output and energy, in CsI(TL) crystals Eq. (3.3) and plastic scintillators Eq. (3.7), to observed signal yields, taking into account the signal mixing described by Eq. (3.5) and (3.6). The fitting routines are using, in principle, ten parameters: $a_{\rm csi}$, $b_{\rm csi}$, $c_{\rm csi}$, $w_{\rm csi}$, $a_{\rm pl}$, $b_{\rm pl}$, $c_{\rm pl}$, $w_{\rm pl}$, $Q^{S}_{\rm mix}$, and $Q^{\rm F}_{\rm mix}$. However, as it was shown in Ref. [67], using specific relationships between the fit parameters, the fit can be reduced to simultaneous fit of only four parameters.

The presented above method can be used for calibration of other types of detectors. The case of phoswich detectors is the most complicated one because of the signal mixing. In the Si–Si or Si–CsI telescopes the signals are independent. Moreover, the dependence between the electronic pulses and the deposited energy is almost linear for silicon detectors. This makes the fitting procedure much more simple.

3.2. The neutron multiplicity detectors

The neutron multiplicity calorimeters are working using the moderation and subsequent diffusion and capture of incoming neutrons. The neutrons are moderated in the liquid scintillator mainly by many-step neutron-proton and neutron-carbon elastic scattering. After moderation, the neutrons diffuse through the scintillator and are captured by Gd component of the doped scintillator [69]. The Gd isotopes have a very high cross-section ($\approx 10^3$ b) for thermal-neutron capture. Simulation performed for ND-309 liquid scintillator with Gd concentration of 0.2% by weight has resulted in neutron capture time distribution extending for over 120 μs, showing the time-scale of the diffusion process [65].

After the moderation and diffusion, the neutrons are captured by the Gd nuclei, what is followed by a cascade of γ-rays. The cascade consists mainly of two or three γ-rays with a total energy of approximately 8.5 MeV. The γ cascade produce a scintillation light which is detected by fast photomultipliers.

The essential role in neutron multiplicity calorimeters is played by the electronics, which handle the photomultiplier signals and record the capture times. During the heavy-ion reaction, a large number of emitted neutrons is simultaneously entering the Gd doped scintillator. Because of the statistical diffusion process the capture times of individual members of the neutron ensemble are, on average, well separated in time. This allows the corresponding light flashes to be counted independently. However, because the members of the same γ cascade can be counted by different multipliers a recording of captures times is necessary to reject multiply counting of the same capture event.

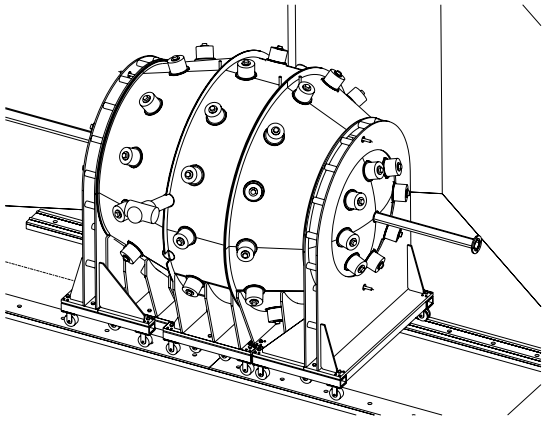

Fig. 7. A perspective view of the SuperBall neutron multiplicity meter in operating configuration [65].

One of practical realizations of the 4π neutron multiplicity calorimeter was the Rochester University 900 liter RedBall [64]. It was used together with the Dwarf BALL/WALL multidetector [61] in the ^{136}Xe+^{209}Bi experiment at 28 MeV/nucleon [5,6]. This relatively small single-element neutron detector allowed one to detect neutrons with efficiency $\varepsilon \approx 0.5$–0.6. Because of the heavy-ion reactions kinematics, most of the neutron emission, having high neutron energies are focused at forward angles. This feature has inspired construction of a segmented neutron multiplicity meter, with thicker forward scintillation layer. This has increased the detection efficiency to $\varepsilon \approx 0.82$ for the new SuperBall detector [65]. The view of the 5-segment, 16000 liter, Rochester SuperBall neutron calorimeter is presented in Fig. 7.

The general characteristic of SuperBall neutron calorimeter is presented in Fig. 8, where the detection efficiency is shown as a function of neutron energy.

As one can see in Fig. 8, the detection efficiency drops down systematically for neutron energies greater than 10 MeV. It falls almost to zero for energies greater than 100 MeV, as the detector thickness is too small to allow for an efficient thermalization of fast neutrons and capture. In the real experiment, the neutron energy has a distribution dependent on the bombarding energy. Table II shows the average detection efficiency in the ^{136}Xe + ^{209}Bi reaction at $E/A = 28$ MeV (RedBall), and 40 and 62 MeV (SuperBall). Because the RedBall detector was much smaller than the SuperBall, to detection efficiency is only 0.52 for 28 MeV case.

During the ^{136}Xe+^{209}Bi experiment, the SuperBall was operating using 128 μs long counting gate. During this period capture times were recorded by the SuperBall Event Handler (SBEH) electronics for all five SuperBall

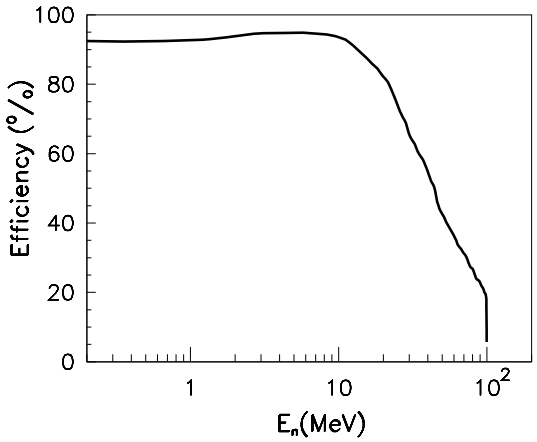

Fig. 8. SuperBall average efficiency of detecting a single neutron with energy E_n. DENIS simulation.

TABLE II

Average efficiency for neutron detection for ^{136}Xe+^{209}Bi reactions at E/A = 28, 40 and 62 MeV, respectively. DENIS simulation.

Energy	28 MeV/nucleon	40 MeV/nucleon	62 MeV/nucleon
Detector	RedBall	SuperBall	SuperBall
Efficiency	0.52	0.65	0.57

segments separately. The counting gate was triggered by a signal from the DWARF BALL/WALL detector, or by the prompt light output produced by neutrons and gamma rays entering the liquid scintillator. Because of the very efficient and sophisticated electronics, it was possible to monitor and eliminate the "cross-talk" between the different SuperBall segments in the "on-line" capture times analysis. The further "off-line" analysis has resulted in a strong reduction of the background and random counts.

Because of the long thermalization times and, hence, a need for a long counting gates, the beam intensity had to be kept low (few hundred counts per second maximum) to avoid event pile-ups.

4. Reaction characteristics in the Fermi energy domain

The proper reaction characteristics is based on identification of particle emission sources. This gives an opportunity to describe the properties of primary fragments created in the early collision stage, and consequently the reaction mechanism. In the experimental reality, one observes not primary, but secondary reaction products. The final (secondary) fragment distributions usually represent an overlap of emission from different sources. The overlap complicates the data interpretation, especially in the case when different fragment emission mechanisms are involved. In heavy-ion collisions at intermediate energies, one observes an overlap of *statistical* emission from the PLF and TLF sources, with *dynamical* emission from the intermediate-velocity source (IVS) [5, 6].

4.1. Dissipative orbiting

The study of correlations between energies and deflection angles of the projectile-like fragments [71] has played a crucial role in gaining an understanding of heavy-ion reaction dynamics both, at low bombarding energies of a few MeV/nucleon above the interaction barrier [2], and at lower boundary of the Fermi-energy [72]. It has been shown [72] that, for this latter energy domain (28 MeV/nucleon) the reaction cross-section is still dominated by dissipative binary reactions involving well defined projectile- and target-like fragments, similar to what is observed at low bombarding energies [2].

Projectile-like fragments emitted in the ^{136}Xe+^{209}Bi reactions at $E/A =$ 28, 40, and 62 MeV, were detected using silicon detector telescopes placed at very forward angles, including the angular region around the grazing angle. In the 28 and 62 MeV/nucleon studies, the PLF telescopes were position sensitive, allowing for an accurate measurement of the PLF emission angle.

The observed "deflection-function plots" of the fragment yield as a function of the energy and the emission angle of PLFs are displayed in Fig. 9 for bombarding energies of $E/A = 28$ and 62 MeV. Fig. 9 presents also several characteristic system trajectories representing elastic (1), grazing (2), moderately damped (3), and negative-angle, orbiting-like (4) collisions. The segments of the deflection-function plots corresponding to these four classes of trajectories are labeled 1 through 4. As seen in Fig. 9, sections of the yield ridges associated with elastic scattering connect regions labeled 1 and 2. For midperipheral collisions, the two colliding heavy ions form a transient dinuclear system and orbit about each other for a fraction of a revolution while dissipating some of their relative kinetic energy. This process is reflected in segments 2–3 and 3–4 of the yield ridges. For the segment connecting areas 2 and 3, the PLF deflection angle is seen to decrease with increasing energy dissipation, reflecting the fact that both, the energy dissipation and the deflection angle are functions of the impact parameter and that with decreasing impact parameter, the former increases while the latter decreases.

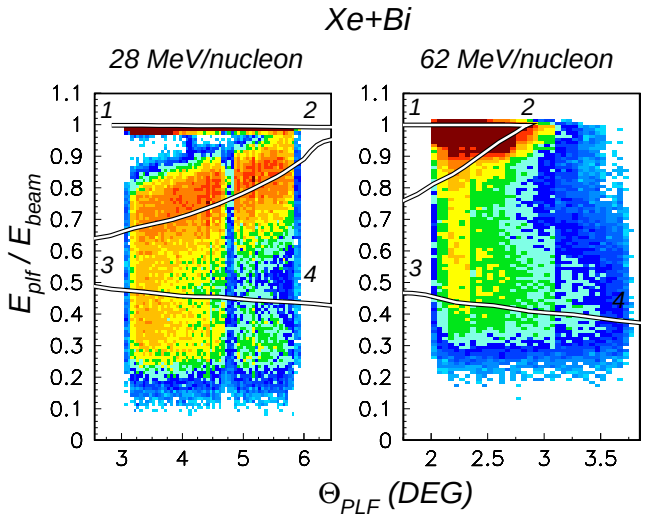

Fig. 9. Comparison of logarithmic contour plots of the PLF yield in a "deflection-function" representation with the results of model calculations (lines), using the stochastic nucleon exchange model CLAT and the equilibrium-statistical decay model GEMINI.

For the segment connecting regions 3 and 4, on the other hand, the deflection angle is seen to increase with increasing energy dissipation and, hence, decreasing impact parameter. This could be simply a result of the experiment being unable to distinguish negative-angle deflection (as in the case of the class-4 trajectories) from that due to positive angles. It is worth noting that there is no conceptual difference between dissipative orbiting leading to either positive or negative deflection angles, the angle of zero degrees playing no special role.

It appears from Fig. 9 that the general collision scenario at $E/A = 62$ MeV is similar to dissipative orbiting followed subsequently by the statistical decay of the primary PLF and TLF fragments, as has been found at lower bombarding energies. Like for lower bombarding energies, most of the reaction cross-section at $E/A = 62$ MeV is associated with binary collisions. Here the term "binary" refers to the primary collision phenomenology and not to the number of reaction products finally observed in a measurement. In view of these observations one is led to conclude that a transition of the reaction mechanism to a potential high-energy scenario dominated by two-body interactions and two-body dissipation must occur at bombarding energies higher than $E/A = 62$ MeV.

The comparison shown in Fig. 9 between data and simulations based on the stochastic nucleon exchange model code CLAT [75][1] combined with the statistical deexcitation model code GEMINI [45] indicates consistency of data with such a theoretical scenario. As seen in this figure, the stochastic nucleon exchange model explains qualitatively the general "topography" of the yield ridges. The model fails, however, to describe quantitatively the lower ridge of the observed pattern. This discrepancy could be due to the fact that only one-body dissipation is included in the CLAT model. Possibly, for high degrees of energy dissipation (midcentral or central collisions) two-body dissipation could also play an important role. These features may also indicate a *different reaction mechanism* operating in the more violent nuclear collisions invalidating basic assumptions of the simulation, where a binary dissipative first reaction stage is well separated in time from the subsequent statistical decay of primary PLFs and TLFs.

4.2. PLF fragmentation — sequential or prompt multifragmentation?

The PLF yield shows a character of predominantly binary dissipative collisions followed by the statistical decay of the primary PLF, as demonstrated in the analysis of the ^{136}Xe+^{209}Bi reaction at bombarding energies of $E/A = 28$, 40, and 62 MeV. However, the likely statistical decay scenario does not exclude all prompt decay alternatives. Analysis of correlations

[1] CLAT presents an approximation of Randrup NEM model [29, 30].

between fragments originating in PLF fragmentation (see Eq. (2.27)) can contribute to a further distinction between binary/sequential and prompt decay scenarios.

The observable differences between the prompt and sequential decay are mainly consequences of the different characteristic time scales for these processes. Prompt (simultaneous) break-up occurs within times of the order of 10 fm/c after initial excitation, while the chain of binary sequential decays lasts from 10 to 10^5 fm/c, depending on the amount of excitation energy. Furthermore, a longer time elapsed between successive binary decays leads to a larger spatial separation and, consequently, to a weaker Coulomb repulsion.

In order to analyze the decay scenarios one first has to identify and select properly the decaying nuclear system, the "source". In the following, experimental data for PLFs will be used, as obtained from a ^{40}Ca+^{40}Ca experiment at 35 MeV/nucleon. The PLF is a natural candidate for an experimental investigation of prevailing decay scenarios since, for a given reaction, one can scan a wide range of possible PLF excitation energies, *e.g.*, by impact parameter event selection.

At relatively high bombarding energies the selection of events corresponding to the PLF fragmentation is aided by reaction kinematics. Particles originating from the PLF fragmentation are focused in a forward angular region and have energies that are mostly well above the detection thresholds. For a PLF study the "well measured" events, *i.e.*, events where most of the emitted particles have been detected, are characterized also by high total longitudinal momentum (parallel to the beam): $P_{||} > 8\,\mathrm{GeV}/c$ (about 80% of the projectile momentum).

Before analyzing the fragment correlations the *primary* PLF has to be reconstructed. Here, the PLF reconstruction is based on an event-by-event routine which uses detected IMFs for reconstructing the velocity vector of the center of mass of the primary PLF [73]. In order to avoid influences from other decay sources (TLF, IVS), only the IMF fragments with velocity larger than the reaction CM velocity are accepted.

The procedure used to reconstruct the primary PLF is applied in a symmetric fashion to the primary simulation data, using the software emulator ("filter") of the experimental set-up. Here, for the ^{40}Ca+^{40}Ca reaction modeling we are using the nucleon exchange random-walk model [32]. The decays of excited PLF and TLF are simulated with the prompt multifragmentation model MULFRA [56] or, alternatively, by the dynamical version of the GEMINI code [59], which was used as partition generator in the MULFRA model.

Fig. 10 presents results of the PLF reconstruction procedure for both, experimental and simulation data. The events were selected with conditions for total multiplicity: $M_{\rm tot}\geq 5$, IMF multiplicity: $M_{\rm IMF}\geq 2$, and the total parallel momentum: $P_{||} > 8\,{\rm GeV}/c$. As one can see, the reconstructed PLF charge (Z) distribution has a mean value around 20 and is quite broad. A broad distribution was also obtained for the PLF excitation energies. As one can see in Fig. 10, the excitation energy distribution has a maximum around 3.5 MeV/nucleon and decreases for smaller and larger values of the excitation energy per nucleon. This is the result of sorting criterion used for the event selection, mainly of the condition that at least two coincident IMFs be emitted in an event. This criterion was applied in order to study IMF-IMF velocity correlations. The fact that the excitation energy distribution extends beyond 10 MeV/nucleon should not be taken at face value. The high-energy tails represent mainly resolution effects originating in uncertainties of the reconstruction procedure caused by incomplete event detection and the related errors in the determination of the reaction Q value.

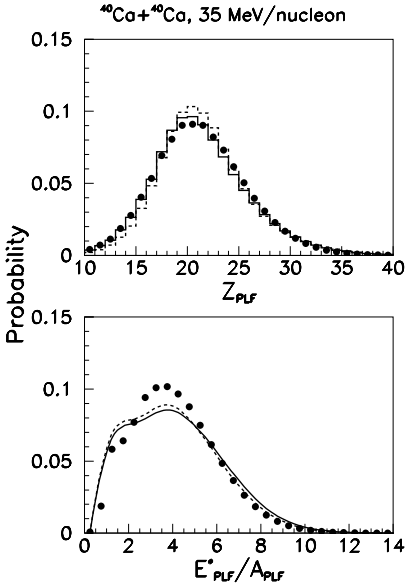

Fig. 10. The reconstructed PLF charge and excitation energy per nucleon distributions. Black dots — experimental data, solid line — prompt multifragmentation simulation, broken line — sequential decay simulation.

The IMF-IMF reduced velocity correlation functions (see Eq. (2.28)) measured for $3 \leq Z \leq 8$, and the corresponding particle charge spectra are shown in Fig. 11 for different bins in primary PLF excitation energy. The reduction of the correlation function ("Coulomb hole") seen at small values of

$v_{\rm red}$ clearly broadens for higher PLF excitation energies. It is a consequence of closer space-time proximity between the emitted IMFs. The sequential binary scenario explains the experimental data at low excitations, below 3 MeV/nucleon only. At higher excitations one has to use a correlation function calculated according to the prompt scenario [74].

As seen from Fig. 11 (right column), good agreement is obtained between measured Z distributions and model predictions, for both sequential and prompt reaction scenarios and for all excitation energy bins.

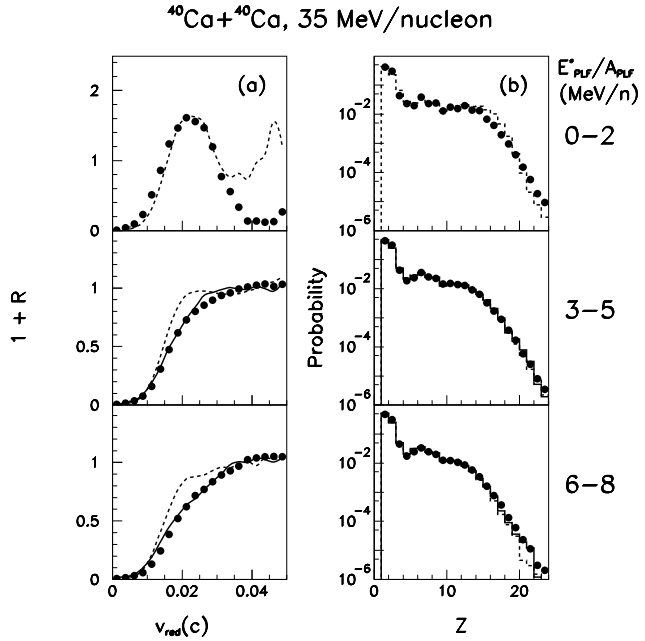

Fig. 11. Reduced velocity correlations for IMFs ($3 \leq Z \leq 8$) emitted from PLF (left panel), and corresponding reaction charge spectra (right panel), for different bins of reconstructed PLF excitation. Black dots — experimental data, solid line — prompt multifragmentation simulation, broken line — sequential decay simulation.

4.3. Particle emission characteristics

The correlations between emitted particles are essential to consider in a study of reaction mechanisms. In spite of many experimental efforts they have generally not been fully explored. This lack is due to the difficulty of simultaneous measurements of charged particles and neutrons in experiments using 4π detectors for charged particles. This difficulty has been overcome only in very few cases, where neutron calorimeters were combined with 4π charged-particle arrays. The present study therefore concentrates

on the available examples of experiments in which correlations between neutrons and charged particles have been measured, such as for the ^{136}Xe+^{209}Bi reaction at three bombarding energies of $E/A = 28$, 40, and 62 MeV [76].

The setups of two separate experiments studying the ^{136}Xe+^{209}Bi system included each a 4π detector system: *(i)* the Washington University charged-particle detector array; Dwarf Ball/Wall [61], *(ii)* the University of Rochester RedBall neutron calorimeter [64] for the 28 MeV/nucleon study, and the SuperBall neutron multiplicity meter [65] for the 40 and 62 MeV/nucleon studies.

The main features of particle emission are well represented by the joint distribution of neutron and light-charged particle (LCP) multiplicities, shown in Fig. 12. The contour plot of yield *versus* neutron and LCP multiplicity shown in this figure is valid for the 62 MeV/nucleon data. It exhibits a characteristically non-linear profile for the ridge of probability. Average ridge profiles are included as solid and open dots, for 28, 40, and 62 MeV/nucleon, respectively. Open stars illustrate theoretical model predictions based on a production mechanism for the primary fragments as described by the classical dynamical code CLAT [75] discussed previously. The subsequent decay of the excited primary fragments was simulated according to the equilibrium-statistical decay model as implemented in the code GEMINI [45].

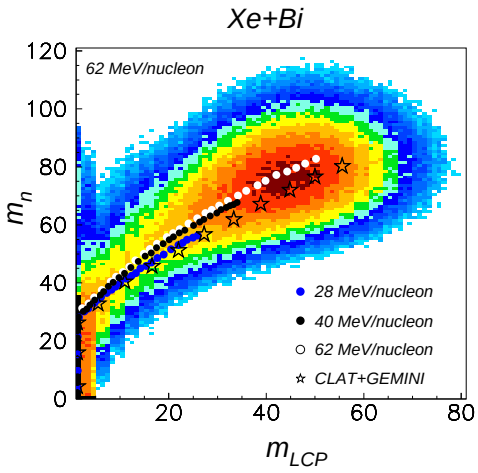

Fig. 12. Logarithmic contour plot of the joint multiplicity distribution plotted *versus* multiplicity of neutrons (m_n) and light-charged particle multiplicity (m_{LCP}) for ^{136}Xe+^{209}Bi reaction at $E/A = 62$ MeV. Symbols represents centroids of slices of the distributions for 28, 40, and 62 MeV/nucleon. Also included are predictions by model calculations for 62 MeV/nucleon (stars). All distributions were corrected for detection efficiency. See Table I and Table II.

The joint multiplicity distribution shown in Fig. 12 provides a important information about the evolution of the reaction with decreasing impact parameter (increasing excitation energy). Its characteristic shape reflects basic features expected for statistical particle emission. Thus, for very peripheral collisions associated with low primary fragment excitations one observes only neutron emission, the ridge segment parallel to the m_n axis ($0 \leq m_n \leq 28$) in Fig. 12. Since neutrons do not have to overcome a Coulomb barrier, they are emitted even at very low excitation energies. On the other hand, light-charged particle emission sets in when the excitation energy is high enough to let charged-particles to pass the barrier (Gamov factor). Then, one observes a non-trivial competition between neutron and LCP emission, which leads to the characteristic bend in the joint multiplicity pattern in Fig. 12.

As one can see from Fig. 12, the theoretical model calculations represent the experimental data quite well. This agreement indicates that the subset of experimental observations included in this figure is consistent with a scenario of predominantly binary dissipative collisions followed by statistical decay of the primary PLF and TLF. However, one notices that the evaporation stage has a dominant influence on the shape of the FINAL experimental fragment distributions. Therefore, the above agreement does not exclude other reaction modes such as the participant-spectator model [77].

The profiles of joint multiplicities of neutron and LCPs shown in Fig. 12, exhibit nearly an invariance with respect to bombarding energy, starting with the same offset for LCP emission. Such invariance is an indication of *thermal scaling*. It can be understood in terms of thermal (*statistical*) emission from equilibrated PLF and TLF sources [78].

The increase of neutron and LCP emission with excitation energy is well illustrated in Fig. 13, where the correlation between the joint multiplicity distribution and the associated total excitation energy per nucleon is shown for combined "CLAT+GEMINI" calculations (middle panel). The results of model calculations were "filtered" by emulating numerically the response of the Dwarf Ball/Wall and the RedBall and SuperBall 4π detector systems to the impinging flux of reaction products. The systematic increase of neutron and LCP emission with system excitation energy exhibits similar distinct correlation pattern for all bombarding energies, supporting *thermal scaling* hypothesis. As it is shown in the bottom panel of Fig. 13, the system excitation energy is strongly correlated with impact parameter ($b_{\max}$ corresponds to grazing angle, defining maximum reaction cross-section). This gives an opportunity to use the joint multiplicity distribution for different impact parameter (excitation energy) regions selection — see the top panel of Fig. 13. In the presented paper four collision regions were selected: *(i)* peripheral collisions, *(ii)* midperipheral collisions, *(iii)* midcentral collisions, and *(iv)* central collisions.

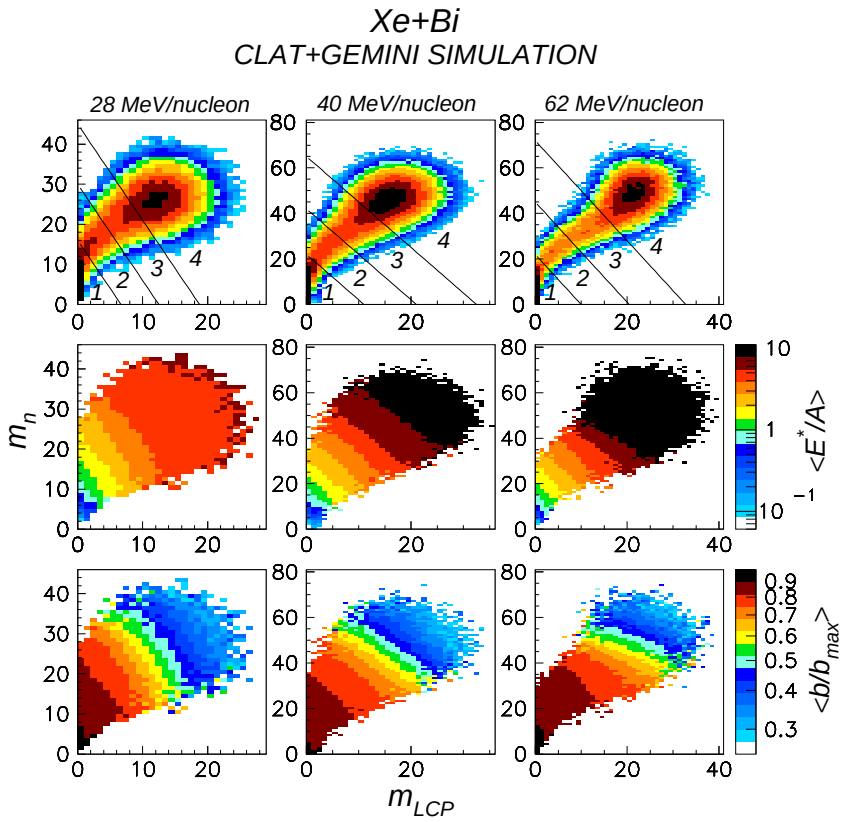

Fig. 13. Logarithmic contour plot of the joint multiplicity distribution (top panel), the associated average total excitation energy per nucleon (middle panel), and the corresponding average impact parameter (bottom panel), for ^{136}Xe+^{209}Bi reactions at $E/A = 28$, 40, and 62 MeV, as predicted by combined "CLAT+GEMINI" models. The model calculations were "filtered" using an experimental set-up emulator.

The correlation between neutrons and LCPs provides information mainly about the hot fragments deexcitation phase, since most of them comes from evaporation from excited fragments. Therefore, an important extension of fragments correlation study can be made by plotting triple correlation between neutrons LCPs and IMFs. An example of such a correlation is presented in Fig. 14, where the average atomic number of IMFs, $\langle Z_{\rm IMF}\rangle$, is presented in a contour diagram plotted *versus* neutron and LCP multiplicities.

As seen in Fig. 14, the $\langle Z_{\rm IMF}\rangle$ increases noticeably and systematically toward higher neutron and LCP multiplicities as the excitation energy increases. Assuming thermal emission, one would expect increase of IMF

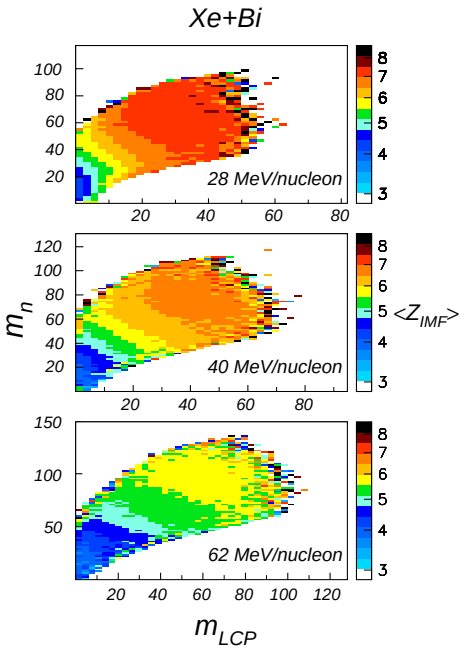

Fig. 14. Experimental logarithmic contour plots of average atomic number of IMFs, $\langle Z_{\rm IMF}\rangle$, as a function of associated neutron and LCP multiplicities as observed in ^{136}Xe+^{209}Bi reactions at E/A = 28, 40 and 62 MeV, respectively. Neutron and LCP distributions were corrected for detection efficiency. See Table I and Table II.

emission with excitation energy. Also, one would expect smaller sizes of IMFs when more LCPs are emitted, according to Z conservation. However, the observed shift of equi-$\langle Z_{\rm IMF}\rangle$ lines is opposite to what is expected. This fact can be explained assuming a prevalence of *dynamical* IMF emission compared to *statistical* evaporation. In the *dynamical* emission one expects a correlation between IMF charge distribution and the size of the overlap (interaction) zone, produced in course of the collision between the projectile and target nuclei. In such a scenario, it is natural to expect a positive correlation of IMF sizes with size of the interaction zone. Further, for similar sizes of the overlap zones (equal $\langle Z_{\rm IMF}\rangle$ in the hypothesis under consideration), the degree of achieved energy damping would increase with increased bombarding energy. This would give a rise to more neutrons and LCPs emission at higher bombarding energy for a fixed $\langle Z_{\rm IMF}\rangle$. As one can see, the latter effect is consistent with experimental patterns in Fig. 14. On the other hand, for higher bombarding energies, a smaller overlap region leads to the same excitation energy of PLF and TLF. Therefore, one observes a shift of equi-$\langle Z_{\rm IMF}\rangle$ lines toward higher excitation energies (higher neutron and LCP multiplicities).

The consistency of observed correlations has been compared with predictions of different theoretical models. Thus classical calculations with the dynamical code CLAT [75] were performed using either the equilibrium-statistical decay code GEMINI [45] or the (pseudo-microcanonical) statistical multifragmentation code SMM [52]. Note that modeling of a complete scenario always requires successive application of interaction phase models, followed by the statistical modeling of the decay of the products emerging from the interaction phase. Such calculations are, of course, based on assumption of statistical character of reaction scenarios and do not include dynamical fragment emission. Therefore, additional calculations with QMD CHIMERA code [24] were performed. In the present version the CHIMERA code includes an isospin dependence of the nuclear interactions. Calculations were made for a soft EOS ($K \approx 200\,\mathrm{MeV}$) and a symmetry energy strength coefficient corresponding to an ASY-STIFF EOS ($C = 31.4\,\mathrm{MeV}$). Typically, calculations with the CHIMERA code were performed for times from $t = 0$ up to $t = 300\,\mathrm{fm}/c$.

When modeling the sequential decay of primary products, a dynamically enhanced version of the GEMINI code [59] was used that incorporates a mutual Coulomb interaction of all emitted particles and the corresponding heavy evaporation residue. In such a modeling, excited primary fragments were allowed to decay in flight with proper time constants, with trajectories of all products being calculated by solving numerically a set of respective equations of motion.

Results of attempts to reproduce the observed correlations by three reaction scenarios are illustrated in Fig. 15, were the experimental data (panels in top row) are followed by three pairs of contour plots for the bombarding energies $E/A = 28$ (left column) and 40 MeV (right column).

As seen in the panels in the second row, the combined "CLAT+GEMINI" results only faintly resemble the experimental trends, consistent with the role of the dynamical component in the IMF yield. This is also not surprising in view of the fact that very few IMFs are expected within the framework of either of the two sub-models.

The third row illustrates the gross failure of the simultaneous multifragmentation model SMM [52] to account for a prominent experimental correlation pattern. Based on an argument presented above regarding a dynamical IMF component, one would not expect a good agreement with experiment in this case, either. However, the predicted correlations for the "CLAT+SMM" scenario are to a good extent even orthogonal to those actually observed. This may be taken as indication of a very small role of simultaneous breakup for IMF emission, as compared to the total IMF production cross-section.

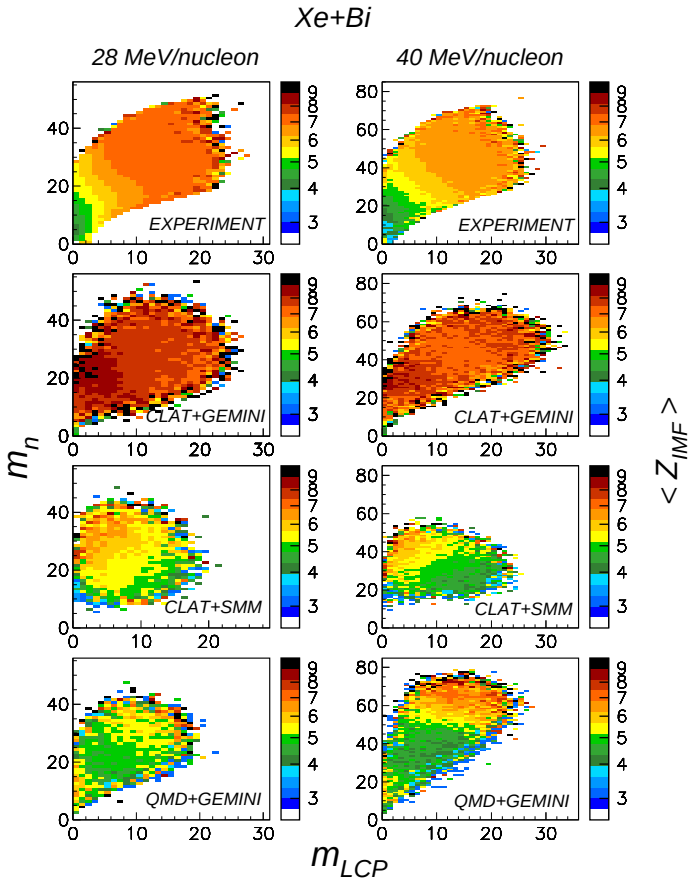

Fig. 15. Logarithmic contour plots of the average atomic number of IMFs, $\langle Z_{\rm IMF}\rangle$, *versus* associated neutron and LCP multiplicities, as observed in ^{136}Xe+^{209}Bi reactions at $E/A = 28$, and 40 MeV. The model calculations were "filtered" using an experimental set-up emulator.

Support for above statement comes from the results of calculations (bottom panels), using the QMD code CHIMERA [24] for modeling the primary reaction stage, followed by decay simulations performed with the dynamical version of the code GEMINI [59]. Even though the CHIMERA scenario predicts too much neutron emission as compared with the LCP yield, it may still be responsible for IMF production in a limited range of impact parameters. This is possible in view of a strong indication that the IMFs, unlike neutrons and LCPs are produced here in dominantly dynamical primary processes, expected to be comparatively well described by a QMD type of code. Indeed, as seen in the bottom panel, CHIMERA is capable to correctly render the trends observed experimentally and, most notably, the increase of average IMF size with increasing neutron and LCP multiplicities.

4.4. Sources of particle emission

The general characteristics of particle emission presented in the previous chapter does not involve selection of particle emission sources. In order to characterize the decay scenarios the emission source have to be properly selected. A common technique of identifying sources of particles emitted in low- and intermediate-energy heavy-ion reactions involves measurement of particle velocities and the subsequent construction of Galilei-invariant distributions of these velocities. Such distributions are conveniently visualized in the form of contour plots of the invariant (renormalized) cross-section in a coordinate system of the velocity components parallel and perpendicular to the beam axis.

The Galilei-invariant velocity plots for ^{40}Ca+^{40}Ca reaction at 35 MeV per nucleon are shown in Fig. 16, for three different bins of impact parameter [79]. Here, as an impact parameter selector the second moment of charge distribution was used — for definition see Ref. [79].

As can be seen in Fig. 16, there are three sources of emitted IMFs. The IMFs emitted in the forward and backward directions, in center of mass system, are corresponding to emission from excited PLF and TLF. The source located close to the center of mass velocity, clearly visible in the bottom panel, corresponds to the intermediate-velocity source (IVS). A small forward shift of the IVS maximum is related to experimental thresholds which are smaller in forward direction (center of mass to laboratory system transformation effect).

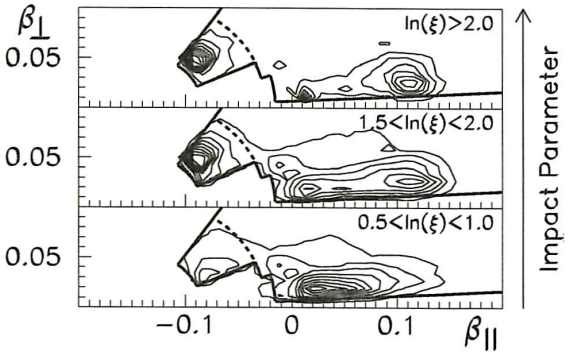

Fig. 16. Logarithmic contour plots of Galilei-invariant velocity distributions ($\beta = v/c$) of intermediate-mass fragments for different reaction (impact parameter) regions for the ^{40}Ca+^{40}Ca reaction at 35 MeV/nucleon. Events selection: $M_{\mathrm{IMF}} = 3$. Solid and dotted lines indicate energy thresholds for $Z = 5$, with and without ionization chambers, respectively [79].

An important observation seen in the evolution of emission sources with the impact parameter is the systematic increase of the IVS emission with increasing collision centrality (decrease of impact parameter). While for peripheral collisions, the emission from excited PLF and TLF prevails over the IVS emission, for central collisions, most of the IMF emission originates from the IVS.

The identification of emission sources is strongly dependent on the detection thresholds. This fact is well illustrated in Fig. 16, where the broken line shows detection threshold for $Z = 5$ in the standard AMPHORA set-up, without ionization chambers. As one can see, without ionization chambers the IMFs emitted from the TLF source located at negative velocities could not be observed.

In the case of ^{40}Ca+^{40}Ca reaction there is also a possibility of composite system (CS) forming, even at intermediate bombarding energies. Although at bombarding energy 35 MeV/nucleon such a probability is very small, it should be taken into account since the CS decay characteristics is similar to that of IVS. In both cases, the emission originates in the center of mass of colliding ions. This fact is illustrated in Fig. 17, where the distributions

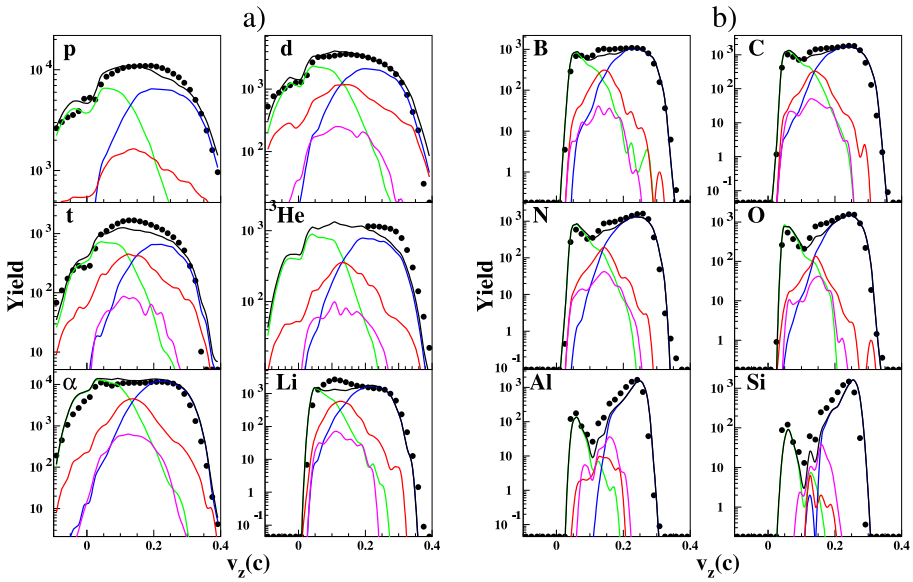

Fig. 17. Distributions of fragments velocity projected on a direction parallel to the beam axis (v_z), for (a) light particles, and (b) intermediate mass fragments, for the ^{40}Ca+^{40}Ca reaction at 35 MeV/nucleon. Black dots: experimental data. Black line: model prediction for total emission. Model predictions for sources: red, blue, and green lines, for model predictions of IVS, PLF, and TLF emission respectively. Violet line: CS contribution. Event selection: $P_{||} > 8$ GeV/c, and $M_{\mathrm{IMF}} \geq 1$ [80].

of fragments velocity projected on a direction parallel to the beam axis, (v_z), are presented for different emission sources [80]. The model calculations were performed with the Sosin stochastic two-stage reaction model [36]. Here, events with total parallel momentum of $P_{||} > 8$ GeV/c and an IMF multiplicity of $M_{\rm IMF}\geq 1$ are accepted as "well-measured" events.

TABLE III

Relative intensities of ejectiles emitted from the PLF, TLF, IVS, and CS sources, predicted by the Sosin model [80], and seen by the AMPHORA system (after experimental set-up emulator). Event selection: $P_{||} > 8$ GeV/c, and $M_{\rm IMF}\geq 1$.

SPECIES	PLF	TLF	IVS	CS
protons	0.443	0.383	0.136	0.038
deuterons	0.373	0.345	0.237	0.045
tritons	0.352	0.345	0.255	0.048
^{3}He	0.390	0.381	0.177	0.052
^{4}He	0.435	0.409	0.134	0.022
carbons	0.644	0.249	0.087	0.019

As can be seen in Fig. 17 the CS component is much weaker than that for IVS — see also Table III. Comparing the widths of the velocity distributions, one can find that the IVS components widths are much broader than those of the CS. This fact is a consequence of different emission mechanisms. The CS decays via the *statistical* emission as the PLF or TLF, while the fragments originating from IVS are produced *dynamically* in the projectile and target overlap region. The dynamical emission is not only a feature of IMFs. As one can see from Fig. 17 and Table III, also light clusters, *i.e.* deuterons, tritons, ^{3}He, and α-particles are to certain extend produced dynamically.

The ^{40}Ca+^{40}Ca system is relatively light. The features of IMF emission can be more clearly observed in collisions of heavier systems, where more IMFs are produced. It is especially important in experiments with such systems as AMPHORA or Dwarf Ball/Wall that have relatively high detection thresholds. Additionally, for systems in which the sum of atomic numbers of projectile and target is greater than that of uranium, the composite system can not be formed in the intermediate bombarding energy range. This avoids ambiguities due to mixing of composite system and IVS components.

These observations provided motivation for a series of experiments on the ^{136}Xe+^{209}Bi system. The characteristics of particle emission sources with dependence on collision centrality are shown in Fig. 18, for three different bombarding energies: 28, 40, and 62 MeV/nucleon. Here, as impact parameter selector the joint neutrons and LCPs multiplicity distribution was used — see Fig. 13.

In the "landscapes" of the plots shown in Figs. 18, three distinct components can be attributed to three emitting effective sources. As seen for peripheral and mid-peripheral collisions there are mainly two sources of emitted particles discernible. They can be identified with fully accelerated PLF and TLF. This picture is largely the same as observed for low energy collisions [2]. The source characteristics change gradually with increasing excitation energy (decreasing of impact parameter). As seen in Fig. 18, a third source of emitted particles with a velocity intermediate between the PLF and TLF velocities first appears and then becomes more and more pronounced, as the associated excitation energy increases. This intermediate-velocity source (IVS) is especially prominent at $E/A = 40$ and 62 MeV. For high bombarding energies, the high relative TLF–PLF velocity allows for a good separation of sources of emitted fragments. An increase in the IMF production rate in the IVS region is seen also for $E/A = 28$ MeV. However, due to the smaller PLF–TLF relative velocity, one observes large overlap of IMF

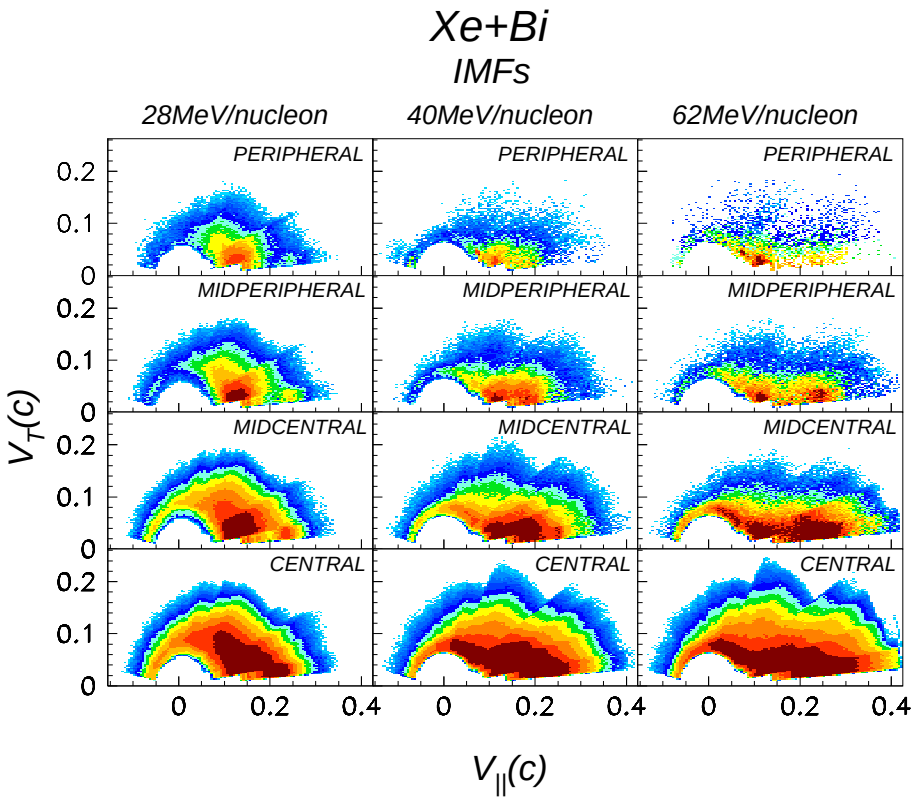

Fig. 18. Logarithmic contour plots of Galilei-invariant velocity distributions of intermediate-mass fragments, different reaction (impact parameter) regions.

emission patterns associated with PLF, TLF and IVS. It is worth noticing that even for peripheral collision one still observes a non-negligible rate of IMF emission.

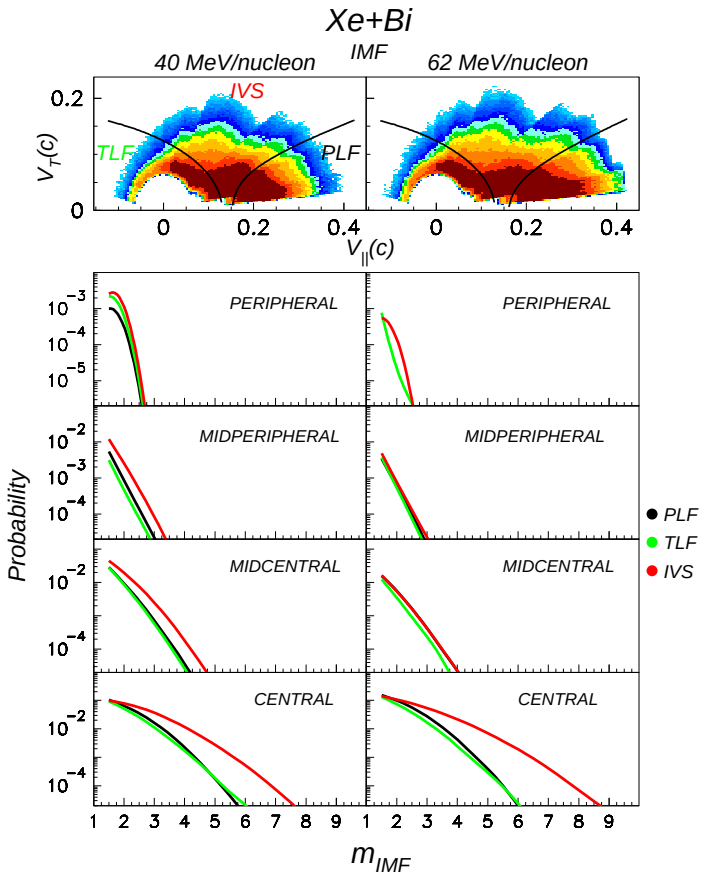

Fig. 19. Multiplicity distributions of IMFs (bottom panels) associated with different decay sources as determined by the source selection criteria depicted by solid lines in the associated Galilei-invariant velocity distributions of the top panels, and "gated" by different bins in the associated reaction (impact parameter) regions.

The different origins of fragment yields can be discerned presenting the yields as Galilei-invariant velocity plots, which achieve kinematical separation of corresponding characteristic emission patterns. Results of such a separation are illustrated in Fig. 19 for the case of intermediate-mass fragments from the ^{136}Xe+^{209}Bi reaction at $E/A = 40$ and 62 MeV. Data from the $E/A = 28$ MeV reaction were not included, since in this case the PLF–TLF relative velocities are too small to provide for a good kinematical separation of the particle yields associated with PLF and TLF sources. The IMF

multiplicity distributions presented in the bottom panels of Fig. 19 were obtained by separating events according to the location of their image on the v_{T} *versus* $v_{||}$ plane relative to the "operational" boundaries for the three sources. Such boundaries are indicated by solid lines in the top panels of Fig. 19.

The probabilities of IMF emission from different sources defined as illustrated in Fig. 19 (top panels) are listed in Table IV. It is clear that such a "raw" selection does not prevent certain degree of misidentification of the particle emission source. Effects of such misidentification decrease with increasing relative TLF–PLF velocity.

TABLE IV

Probabilities of IMF emission from different sources in selected reaction regions (BINS) see Fig. 19, for ^{136}Xe+^{209}Bi reactions at $E/A = 40$ and 62 MeV, respectively.

BIN	Region	40 MeV/nucleon			62 MeV/nucleon		
		$p_{\mathrm{IMF}}^{\mathrm{PLF}}$	$p_{\mathrm{IMF}}^{\mathrm{TLF}}$	$p_{\mathrm{IMF}}^{\mathrm{IVS}}$	$p_{\mathrm{IMF}}^{\mathrm{PLF}}$	$p_{\mathrm{IMF}}^{\mathrm{TLF}}$	$p_{\mathrm{IMF}}^{\mathrm{IVS}}$
1	peripheral	0.17	0.39	0.44	0.19	0.47	0.34
2	midperipheral	0.22	0.31	0.47	0.28	0.30	0.42
3	midcentral	0.28	0.26	0.46	0.34	0.26	0.40
4	central	0.31	0.26	0.43	0.32	0.26	0.42

It is worth comparing Table IV for the ^{136}Xe+^{209}Bi reaction at 40 MeV/nucleon with the bottom row of Table III for ^{40}Ca+^{40}Ca reaction at 35 MeV/nucleon. Although these tables were made for different selections and conditions (Table IV for experimental data, Table III for simulation data), one notices for the heavier system a relatively large probability for IMF emission from the IVS. This enhanced emission can, to some extent, be explained by the geometry of the transient dinuclear system formed in a heavy-ion reaction. For heavier colliding systems the geometrical overlap for a given impact parameter region is larger than that for lighter systems. Similar effects can be observed for any reaction. The scaling of IMF emission with the geometrical overlap of the colliding ions should result in an increase of IMF emission with increased collision centrality or decreased impact parameter. In fact, such an effect is observed for the ^{136}Xe+^{209}Bi reaction, see Fig. 19 and Table IV.

The energy spectra are commonly used for an evaluation of source temperatures. Fig. 20 presents the apparent source temperatures for PLF and IVS sources, for peripheral and central collisions. The temperature parameter, T_{s}, was extracted from slopes of energy spectra in the decaying source frame, assuming Maxwell–Boltzmann-type distribution:

$$P(E)dE \propto \sqrt{E - V_{\mathrm{B}}} \exp\left(-\frac{E - V_{\mathrm{B}}}{Ts}\right) dE\,, \tag{4.1}$$

where E is the energy of the specified particle and V_{B} is energy of the Coulomb barrier.

As a result, the energy spectra can be quantified in terms of inverse logarithmic slope parameters or effective source temperatures, T_{s}. The results of such evaluations for ^{136}Xe+^{209}Bi reactions at three bombarding energies are presented in Fig. 20 for protons, alpha particles and lithium IMFs.

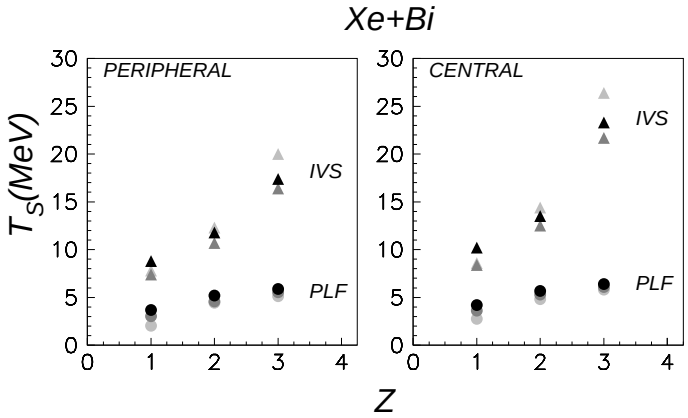

Fig. 20. Apparent temperatures for ^{136}Xe+^{209}Bi reactions at E/A = 28 (grey), 40 (dark-grey) and 62 MeV (black), respectively. Temperature parameters were extracted from slopes of energy distribution of protons (Z = 1), alphas (Z = 2) and Li (Z = 3) fragments in the emission source velocity frame of PLF (circles) and reaction center-of-mass (IVS)–triangles, respectively (see text). Events were selected for different bins in the associated reaction (impact parameter) regions: PERIPHERAL (BINS 1 and 2), and CENTRAL.

Here, bins 1 and 2 for peripheral collisions, were added in order to increase statistics. In order to decrease the misidentification of emission sources, the fragments were selected in the forward and backward hemispheres defined with respect to the source velocity vectors for PLF and TLF, respectively. Fragments from the IVS zone were selected in the thin slice around the center-of-mass velocity.

As can be seen in Fig. 20 the apparent source temperatures are much higher for clusters (α-particles and IMFs) emitted from the IVS source, as compared to the PLF source. In fact, the apparent IVS cluster temperatures are much too high for statistical emission. Such "hard" (high temperature) spectra can be explained only by assuming dynamical (non-equilibrium) emission from an IVS source. While the temperatures of LCPs and IMFs

emitted from the PLF are similar, the temperature of IMFs (here $Z = 3$) emitted from the IVS is much higher. This effect can be explained by an admixture of IMFs from the IVS source. It would suggest a dominantly dynamical IMF production. One notices a small increase of source temperatures with increasing bombarding energy, except for the IVS temperatures for the 28 MeV/nucleon reaction. As already mentioned, for $E/A = 28$ MeV/nucleon the relative PLF–TLF velocity is too small for a good separation of the IVS zone from both the PLF and TLF emission regions (see Fig. 18).

5. Summary and conclusions

The general characteristics of heavy-ion collisions at intermediate energies is similar to that observed for low energies and understood in terms of dissipative binary collisions. Thus, at a bombarding energy of 62 MeV/nucleon, the reaction cross-section appears still dominated by dissipative binary reactions involving the survival of well-defined projectile- and target-like fragments.

At intermediate energies, the emission from excited PLF and TLF sources, observed in joint distribution of neutron and LCP multiplicities, shows a *thermal scaling* with bombarding energy, indicating *statistical* emission from equilibrated sources. The analysis based on PLF reconstruction indicates that, as compared to the total reaction cross-section, the PLF and consequently TLF, deexcite mainly via binary sequential decay. However, for excitations above 3 MeV/nucleon, a transition from sequential to prompt multifragmentation is observed.

On the other hand, emission sources identification based on analysis of Galilei-invariant velocity plots show clearly the existence of a third intermediate-velocity source in addition to the PLF and TLF sources. In contrast to the dominantly *statistical* emission from the PLF and TLF, fragments emitted from the IVS are likely to be produced *dynamically* in the overlap zone of the projectile and target nuclei. For central collisions, the IVS component becomes dominant in the IMF production, representing the overlap region of PLF and TLF. Although, for peripheral collision still one observes non-negligible emission rate, with clear IVS component. The analysis of apparent temperatures of fragments energy spectra has revealed that the fragments emitted from the IVS exhibit "hard" (high temperature) spectra, which can be explained only assuming a dynamical (non-equilibrium) emission scenario.

The comparison between IMF emission for relatively light (^{40}Ca+^{40}Ca) and heavy (^{136}Xe+^{209}Bi) systems has shown that the dynamical IMF emission increases for heavier systems, reflecting the geometrical overlap of projectile and target.

Concluding, in the intermediate energy region one observes a mixture of *statistical and dynamical multifragmentation processes.* An analysis of fragment emission patterns has then to be related to proper selection of decay sources, as the fragmentation mechanisms are different for PLF/TLF and IVS. The analysis of (^{136}Xe+^{209}Bi) reaction at 28, 40, and 62 MeV/nucleon has shown that the selection of emission sources, based on kinematical separation, improves with increasing bombarding energy, as it is dependent on relative projectile-target velocity.

The analysis of multidimensional particle correlations between different emitted particles indicates an importance of experiments based on simultaneous detection of neutrons and charged particles in 4π detector configurations. The triple neutron–LCP–IMF correlation, on the other hand, has shown the lack in proper reproduction of basic trends in experimental data by most of prominent theoretical models. This may be an indication of problems with proper modeling of dynamical fragment production at intermediate energies, taking into account relatively good reproduction of experimental data for low bombarding energies.

The failure of reproduction of multidimensional particle correlations by QMD models may then be connected with cluster formation mechanism. In the QMD models a spatial or phase-space proximity criterium for cluster definition is used. An introduction of thermodynamical (entropy) probabilities for cluster formation process might improve the modeled clusterization mechanism. A hint for such solution comes from the Sosin model where the thermodynamical probabilities were introduced to PLF, TLF, and IVS formation. The PLF or TLF can be conceptually treated in the same way as other clusters.

This work was supported by the Polish Ministry of Science and Higher Education under the contact N N202 035636.

REFERENCES

[1] J. Błocki *et al., Ann. Phys.* **113**, 330 (1978).

[2] *E.g.*: W.U. Schröder, J.R.Huizenga, *Treatise on Heavy-Ion science*, Plenum Press, New York and London 1984, Vol.2, p.113–726.

[3] Y. Yariv, Z. Fraenkel, *Phys. Rev.* **C20**, 1291 (1979); J. Cugnon, *Phys. Rev.* **C22**, 1885 (1980); *Nucl. Phys.* **A387**, 191c (1982).

[4] W.U. Schröder, *Nucl. Phys.* **A538**, C439 (1992).

[5] J. Tõke *et al., Nucl. Phys.* **A583**, 519 (1995).

[6] J. Tõke *et al., Phys. Rev. Lett.* **77**, 3514 (1996).

[7] J. Randrup, S.E. Koonin, *Nucl. Phys.* **A356**, 223 (1981).

[8] J. Bondorf *et al., Nucl. Phys.* **A443**, 321 (1985); *Nucl. Phys.* **A444**, 460 (1985).
[9] D.H.E. Gross, *Phys. Rep.* **279**, 119 (1997).
[10] See *e.g.* W. Trautmann, *Nucl. Phys.* **A752**, 407c (2005).
[11] G. Betrsch, P.J. Siemens, *Phys. Lett.* **B126**, 9 (1983).
[12] Ph. Chomaz *et al., Nucl. Phys.* **A583**, 305 (1995).
[13] W. Bauer *et al., Phys. Rev. Lett.* **69**, 1888 (1992).
[14] G.F. Burgio, Ph. Chomaz, J. Randrup, *Phys. Rev. Lett.* **69**, 885 (1992).
[15] L. Stuttgè *et al., Nucl. Phys.* **A539**, 511 (1992).
[16] P. Bonche, S. Koonin, J.W. Negele, *Phys. Rev.* **C13**, 1226 (1976).
[17] J. Aichelin, G. Bertsch, *Phys. Rev.* **C31**, 1730 (1985); K. Morawetz *et al., Phys. Rev.* **C63**, 034619 (2001).
[18] H. Kruse *et al., Phys. Rev.* **C31**, 1770 (1985).
[19] M. Colonna *et al., Nucl. Phys.* **A583**, C525 (1995).
[20] G.F. Burgio, Ph. Chomaz, J. Randrup, *Phys. Rev. Lett.* **69**, 885 (1992).
[21] C. Dorso, J. Randrup, *Phys. Lett.* **B232**, 29 (1989); M.J. Ison, C.O. Dorso, *Phys. Rev.* **C71**, 064603 (2005).
[22] M. Papa, T. Maruyama, A. Bonasera, *Phys. Rev.* **C64**, 024612 (2001).
[23] J. Aichelin, *Phys. Rep.* **202**, 233 (1991).
[24] J. Łukasik *et al., Phys. Rev.* **C55**, 1906 (1997).
[25] E. Plagnol *et al., Phys. Rev.* **C61**, 014606 (2000).
[26] D.H. Boal, J.N. Glosli, *Phys. Rev.* **C38**, 1870 (1988).
[27] A. Uno, H. Horiuchi, *Phys. Rev.* **C53**, 2958 (1996).
[28] H. Feldmeier, *Nucl. Phys.* **A515**, 147 (1990); *Nucl. Phys.* **A586**, 493 (1995).
[29] J. Randrup, *Nucl. Phys.* **A307**, 319 (1978).
[30] J. Randrup, *Nucl. Phys.* **A327**, 490 (1979); **A383**, 468 (1982).
[31] A.J. Cole, *Z. Phys.* **A322**, 315 (1985); *Phys. Rev.* **C35**, 117 (1987).
[32] Z. Sosin *et al., Acta Phys. Pol. B* **25**, 1601 (1994); Z. Sosin *et al., Nucl. Phys.* **A574**, 474 (1994).
[33] L. Tassan-Got, C. Stéphan, *Nucl. Phys.* **A524**, 121 (1991).
[34] D. Durand, *Nucl. Phys.* **A541**, 266 (1992).
[35] J. Błocki *et al., Acta Phys. Pol. B* **21**, 1513 (2000).
[36] Z. Sosin, *Eur. Phys. J.* **A11**, 311 (2001).
[37] L.G. Moretto, *Nucl. Phys.* **A247**, 211 (1975).
[38] W.J. Świątecki, *Aust. J. Phys.* **36**, 641 (1983).
[39] S. Das Gupta *et al., Phys. Rev.* **C35**, 556 (1987).
[40] S. Das Gupta *et al., Phys. Rev.* **C33**, 1634 (1986).
[41] J.P. Blaizot, D. Gogny, B. Grammaticos, *Nucl. Phys.* **A265**, 315 (1976).
[42] V. Baran *et al., Nucl. Phys.* **A632**, 287 (1998).
[43] K. Chen *et al., Phys. Rev.* **166**, 949 (1968).
[44] J. Łukasik, Z. Majka *Acta Phys. Pol. B* **24**, 1959 (1993).

[45] R.J. Charity *et al., Nucl. Phys.* **A483**, 391 (1988).
[46] T. Kozik *et al., Z. Phys.* **A326**, (1987) 421; K. Grotowski *et al., Phys. Lett.* **B223**, 287 (1989).
[47] D. Durand, unpulished.
[48] H. Hauser, H. Feschbach, *Phys. Rev.* **87**, 366 (1952).
[49] V.F. Weisskopf, D.H. Ewing, *Phys. Rev.* **57**, 472 (1940).
[50] J. Randrup, S.E. Koonin, *Nucl. Phys.* **A356**, 223 (1981).
[51] S.E. Koonin, J. Randrup, *Nucl. Phys.* **A471**, 335c (1987); *Nucl. Phys.* **A474**, 173 (1987).
[52] J.P. Bondorf *et al., Phys. Rep.* **257**, 133 (1995).
[53] N. Metropolis *et al., J. Chem. Phys.* **21**, 1087 (1953).
[54] W.A. Friedman, *Phys. Rev. Lett.* **60**, 2125 (1988); *Phys. Rev.* **C42**, 667 (1990).
[55] W. Gawlikowicz, K. Grotowski, *Acta Phys. Pol. B* **22**, 885 (1991).
[56] W. Gawlikowicz, K. Grotowski, *Nucl. Phys.* **A551**, 73 (1993).
[57] H.R. Jaqaman *et al., Nucl. Phys.* **A514**, 327 (1990).
[58] B. Borderie, *Ann. Phys. (Paris)* **17**, 349 (1992).
[59] W. Gawlikowicz, *Acta. Phys. Pol. B* **28**, 1687 (1997).
[60] D. Drain *et al., Nucl. Instrum. Methods* **A281**, 528 (1989).
[61] D.W. Stracener *et al., Nucl. Instrum. Methods* **A294**, 485 (1990).
[62] J. Pouthas *et al., Nucl. Instrum. Methods* **A357**, 418 (1995).
[63] S. Aiello *et al., Nucl. Phys.* **A583**, 461 (1995).
[64] S.P. Baldwin, Ph.D. thesis, University of Rochester, Rochester, New York 1994.
[65] W.U. Schröder, REPORT DOE/ER/79048-1, 1995.
[66] T. Barczyk *et al., Nucl. Instrum. Methods* **A364**, 311 (1995).
[67] W. Gawlikowicz, J. Tõke, W.U. Schröder, *Nucl. Instrum. Methods* **A491**, 181 (2002).
[68] P. Pawłowski, W. Gawlikowicz *et al., Z. Phys.* **A357**, 387 (1997).
[69] B.C. Diven *et al., Phys. Rev.* **109**, 144 (1958); D. Pade *et al., Phys. Rev.* **C43**, 1288 (1991).
[70] B.M. Quednau, University of Rochester, unpublished.
[71] J. Wilczyński, *Phys. Lett.* **B47**, 124 (1973).
[72] S.P. Baldwin *et al., Phys. Rev. Lett.* **74**, 1299 (1995).
[73] R. Płaneta, W. Gawlikowicz *et al., Eur. Phys. J.* **A11**, 297 (2001).
[74] W. Gawlikowicz *et al., Nucl. Phys.* **A681**, 295c (2001).
[75] W.U. Schröder *et al., Nucl. Science Research Conf. Series* **11**, 255 (1986).
[76] W. Gawlikowicz *et al.*, Proceedings of the 11th International Conference on Reaction Mechanisms, Varenna 2006, p. 261.
[77] *E.g.* O. Dorvaux *et al., Nucl. Phys.* **A651**, 225 (1999).
[78] J. Tõke, *et al., Phys. Rev.* **C63**, 024604 (2001).
[79] P. Pawłowski, W. Gawlikowicz *et al., Phys. Rev.* **C57**, 1771 (1998).
[80] Z. Sosin, W. Gawlikowicz *et al., Eur. Phys. J.* **A11**, 305 (2001).